Possible links between extreme oxygen perturbations and the Cambrian radiation of animals

Tianchen He[1,2]*, Maoyan Zhu[3,4], Benjamin J.W. Mills[2], Peter M. Wynn[5], Andrey Yu. Zhuravlev[6], Rosalie Tostevin[7], Philip A. E. Pogge von Strandmann[1], Aihua Yang[8], Simon W. Poulton[2], Graham A. Shields[1]

[1]London Geochemistry and Isotope Centre (LOGIC), Institute of Earth and Planetary Sciences, University College London and Birkbeck, University of London, London, WC1E 6BT, UK.

[2]School of Earth and Environment, University of Leeds, Leeds, LS2 9JT, UK.

[3]State Key Laboratory of Palaeobiology and Stratigraphy & Center for Excellence in Life and Paleoenvironment, Nanjing Institute of Geology and Palaeontology, Chinese Academy of Sciences, Nanjing, 210008, China.

[4]College of Earth Sciences, University of Chinese Academy of Sciences, Beijing, 100049, China.

[5]Lancaster Environment Centre, Lancaster University, Lancaster, LA1 4YQ, UK.

[6]Department of Biological Evolution, Faculty of Biology, Lomonosov Moscow State University, Leninskie gory 1(12), Moscow 119234, Russia.

[7]Department of Earth Sciences, University of Oxford, Oxford, OX1 3AN, UK.

[8]State Key Laboratory for Mineral Deposits Research, School of Earth Sciences and Engineering, Nanjing University, Nanjing, 210093, China.

*e-mail: T.He@leeds.ac.uk

The role of oxygen as a driver for early animal evolution is widely debated. During the Cambrian explosion, episodic radiations of major animal phyla occurred coincident with repeated carbon isotope fluctuations. However, the driver of these isotope fluctuations and potential links to environmental oxygenation are unclear. Here, we report high-resolution carbon and sulphur isotope data for marine carbonates from the southeastern Siberian Platform that document the canonical explosive phase of the Cambrian radiation from ~524 to ~514 Myr ago. These analyses demonstrate a strong positive covariation between carbonate $\delta^{13}C$ and carbonate-associated sulphate $\delta^{34}S$ through five isotope cycles. Biogeochemical modelling suggests that this isotopic coupling reflects periodic oscillations in atmospheric O_2 and the extent of shallow ocean oxygenation. Episodic maxima in the biodiversity of animal phyla directly coincided with these extreme oxygen perturbations. Conversely, the subsequent Botoman–Toyonian animal extinction events (~514 to ~512 Myr ago) coincided with decoupled isotope records that suggest a shrinking marine

sulphate reservoir and expanded shallow marine anoxia. We suggest that fluctuations in oxygen availability in the shallow marine realm exerted a primary control on the timing and tempo of biodiversity radiations at a crucial phase in the early history of animal life.

The early Cambrian witnessed a dramatic diversification of animal body plans and behaviours[1], as well as between-species interactions and palaeocommunity innovations[2,3], ultimately leading to modern animal ecosystems. Ocean oxygenation is a commonly invoked environmental pre-requisite[4–6]. However, some recent studies suggest that despite probable low-oxygen conditions, the oceans exceeded requisite oxygen thresholds for simple animals, such as sponges, well before the Cambrian Period[7,8]. Many of the new animal body plans and lifestyles that appeared during the early Cambrian were associated with considerably higher oxygen demands[9,10]. Fluctuations in the maximum dissolved oxygen content of surface waters, or the extent of shallow ocean oxygenation, could therefore have played an important role in regulating the pattern of Cambrian radiations. This brings into question the role of oxygen in early animal evolution, which is exacerbated by a lack of convincing evidence for a direct link between Earth's oxygenation history and early Cambrian bio-radiations and extinctions[11].

High-resolution records of the sulphur and carbon cycles, when considered in the context of the fossil record may, however, afford an opportunity to resolve potential environmental controls on early animal evolution. The marine biogeochemical sulphur and carbon cycles interconnect via their respective redox-sensitive reservoirs and fluxes. Both elements have a single, large oxidised oceanic reservoir (dissolved sulphate and inorganic carbon), the isotopic composition of which is governed by isotope fractionation during microbially-mediated reduction to sulphide (ultimately preserved as pyrite) and organic carbon. Burial of these reduced species represents the two main net sources of oxygen to the surface environment[12–14], and also imprints on both the seawater sulphate sulphur isotope ($\delta^{34}S$, as recorded by carbonate-associated sulphate) and carbon isotope ($\delta^{13}C$, as recorded in carbonate) records, allowing redox changes in the surface environment to be traced through geologic time.

Here we present paired carbon and sulphur isotope data from lower Cambrian marine carbonates from the southeastern Siberian Platform. These data provide a continuous, high-resolution record from Cambrian Stage 2 through to Stage 4 (~524–512 Myr ago; Fig. 1), and allow a direct assessment of potential links between ocean redox variability, atmospheric oxygenation, and the major biological events of the early Cambrian.

Carbon and sulphur isotope systematics

Carbonate $\delta^{13}C$ and carbonate-associated sulphate $\delta^{34}S$ analyses (see Methods) were primarily performed on well-preserved micritic limestone samples collected from sections along the Aldan and Lena rivers in Siberia. These sections archive a continuous and highly fossiliferous sedimentary record from a shallow, open ocean carbonate platform, and preserve over half of all fossil diversity currently known from the Cambrian radiation interval worldwide, thus providing a unique window into early Cambrian shallow marine ecosystems (see Supplementary Information for geological and palaeontological context, sample details, diagenesis evaluation and all data).

Our carbon isotope data record five cycles through Stage 2 and Stage 3 of the lower Cambrian. Positive excursions are labelled here as III to VII (Fig. 1), consistent with previous studies of the Siberian Platform[15,16], but these excursions are also found elsewhere[17,18]. The new sulphur isotope data range from +16‰ to +36‰, demonstrating that seawater sulphate $\delta^{34}S$ values fell from a peak (~40–45‰) during the late Ediacaran[19,20] to lower values by the early Cambrian. Significantly, these data also demonstrate for the first time that oceanic sulphate $\delta^{34}S$ values varied across five cycles that directly correlate with excursions in seawater $\delta^{13}C$ (Fig. 1; see Supplementary Table S1 for statistical correlation parameters). In sharp contrast to the coupled $\delta^{13}C$-$\delta^{34}S$ trends during the Cambrian stages 2-3, the $\delta^{34}S$ trend across the early Cambrian Stage 4 Botoman–Toyonian extinctions (BTE; the first animal mass extinction of the Phanerozoic Eon)[21,22] is characterised by rapid fluctuations of large magnitude that are decoupled from the carbon isotope record (Fig. 1).

Over long timescales the excess oxidant generated by increased organic carbon burial (as indicated by higher carbonate $\delta^{13}C$) may be balanced by reduced rates of pyrite burial (lower seawater sulphate $\delta^{34}S$), and vice-versa, which results in relatively stable atmospheric oxygen levels and an inverse relationship between the first-order global seawater $\delta^{13}C$ and $\delta^{34}S$

records[23,24]. However, the positive correlations we observe between $\delta^{13}C$ and $\delta^{34}S$ in Cambrian stages 2–3 likely reflect higher rates of both organic carbon and pyrite sulphur burial, which may have been associated with large distinct pulses in atmospheric oxygenation, as previously suggested for the late Cambrian SPICE (Steptoean Positive C-isotope Excursion) event[14].

The rate of change of seawater sulphate sulphur isotope ratios allows us to estimate marine sulphate concentrations through this interval. Using the 'rate method' model[25,26] (see Methods for model details), and taking the average values of the lower end of the data envelopes shown in Supplementary Fig. S2, an upper estimate can be obtained for marine sulphate of ~1.0–6.6 mM for the interval from ~524 to ~514 Myr ago, followed by ~0.4–1.4 mM for ~514 to 512 Myr ago. Estimates for the earlier interval are broadly consistent with previously modelled estimates of ~5–10 mM[25] and with fluid inclusion-based estimates of ~4.5–11 mM for the early Cambrian[27], but trend toward lower values. Thus, the early Cambrian ocean was characterized by a relative paucity of sulphate, when compared with the modern ocean (~28–29 mM). Our data document a significant drawdown of more than half of the sulphate pool during early Cambrian Stage 4 (~514–512 Myr ago), coincident with the BTE.

Environmental oxygenation and animal radiations

The covariant behaviour of the carbon and sulphur isotope systems during Cambrian Stage 2 to late Stage 3 can be explained by coupled burial of pyrite and organic carbon in marine sediments under highly productive, anoxic conditions[23,28,29]. Such conditions result in enhanced preservation and burial of organic carbon, and simultaneously enhance microbial sulphate reduction (MSR), leading to a high pyrite burial flux. Since pyrite and organic carbon are enriched in the lighter isotopes (^{32}S and ^{12}C respectively), elevated burial fluxes on a global scale would drive the positive excursions in seawater sulphate $\delta^{34}S$ and inorganic $\delta^{13}C$.

A biogeochemical box model[12,30,31] (see Methods for model details) was applied to test whether measured trends in S isotopes can be reproduced from the coupled burial of sulphur (as pyrite) and carbon (as organic carbon). The model infers the rate of organic carbon burial using the $\delta^{13}C$ record and an isotopic mass balance, while the rate of pyrite burial is calculated by assuming a linear relationship with organic carbon burial, allowing prediction of $\delta^{34}S$ values. Results (Fig. 2c) show that both the amplitude of positive sulphur isotope excursions and their long-term trend from ~524–514 Ma can be replicated in this way. The model assumes that the isotopic composition of carbon and sulphur inputs ($\delta^{13}C_{in}$, $\delta^{34}S_{in}$), and the background carbon and sulphur cycle input fluxes through weathering and metamorphism remained constant. Variations in these processes may help to explain the slight drift of the baseline $\delta^{34}S$ in model average predictions when compared to the observed $\delta^{34}S$ data. The shaded areas in Fig. 2 show the result of varying $\delta^{13}C_{in}$ between -5‰ and -8‰, allowing the model to encompass most of the data. Our model requires a low concentration of sulphate in seawater (best-fit shown is 1 mM), in order to match the rate and amplitude of $\delta^{34}S$ variations, consistent with the lower end of maximum estimates derived from the 'rate method' model.

The coupled carbon and sulphur isotope swings show repeated cycles of approximately 0.5–2 Myrs duration that reflect cyclical changes in the burial rates of organic carbon and pyrite, which may have been induced by episodic expansion of bottom-water anoxia/euxinia on the deeper portions of continental shelves and slopes. Ultimately, coupled burial of both reduced species in marine sediments results in the release of oxygen and other marine oxidants[14]. Each rising limb and the peak of the positive isotope swing thus represents enhanced net oxygen production and a pulse of atmospheric oxygen, which initially increased the extent of oxygenated waters and/or the maximum dissolved O_2 in the shallower realm. Subsequently, increased ventilation of the deep ocean would have resulted in a reduced flux of reductant (organic carbon and pyrite) to seafloor sediments[32]. This acted to decrease the net oxidant flux, which ultimately buffered against further oxygenation. Furthermore, positive feedbacks between ocean ventilation and phosphorus retention in sediments[33] may have driven rapid bottom-water oxygenation, and in this case the decrease in the net oxidant flux may be substantial, leading to a re-establishment of anoxia, and potentially giving rise to the repetitive isotope cycles[33].

Alternatively, isotope cyclicity might be driven by orbital forcing via climatic impacts on weathering, similar to the ~1–2 Ma "third-order" eustatic sequences of the Mesozoic and Cenozoic Eras[34]. However, neither the timing, duration and frequency of early Cambrian third-order sea-level fluctuations[18,35], nor regional sequence stratigraphy data from Siberia[36]

(Supplementary Table S3), appear to match the isotope cycles identified in this study. Similarly, an erosional driver[37] for the observed isotope cycles is incompatible with their combined high amplitude and frequency, which would require very large (~3-5 fold[37]) changes in global erosion over geologically-short timescales. Furthermore, an erosional driver is not supported by contemporaneous changes in seawater $^{87}Sr/^{86}Sr$[38]. Fluctuations in oxygen minimum zone depth[39,40], alongside biological feedbacks such as enhanced diurnal vertical migration via increased expansion of metazoan mobility[41], may also have contributed to the perturbations in shallow ocean oxygenation.

To summarize, our model indicates the potential for large variations in the net atmospheric oxygen production flux (±50% around the baseline value; Fig. 2d). We propose that periods of rising $\delta^{13}C$ represent enhanced burial of reductants under anoxic bottom-water conditions and atmospheric oxygenations, whereas the falling limbs record the decrease of reductant burial under a more widely oxygenated deep ocean. A more direct estimate of oxygen production rates can be made within our model by treating both $\delta^{13}C$ and $\delta^{34}S$ as input parameters, thus inferring rates of organic carbon and pyrite burial, respectively, for the time points where we have input information for $\delta^{34}S$. These estimates are shown in Fig. 3 and are similar in magnitude to those of the carbon-only model, which is to be expected as the carbon-only model produced a reasonable fit to the $\delta^{34}S$ data.

One direct impact of pulses in atmospheric oxygenation during the early Cambrian was episodic oxygenation of marginal shallow marine environments. Shallow carbonate platforms, such as the Aldan-Lena rivers region, evidence relatively high animal origination rates and biodiversity[42,43]. Within shallow ocean ecosystems, biogenic reefs serve as critical evolutionary cradles and net sources of marine biodiversity[44]. Comparing the isotopic cycles and estimated oxygen production curves with species diversity curves for the Siberian Platform (see Supplementary information for full palaeontological data), oxygenation pulses (III, IV, V, VI, VII) generally coincided with regional biodiversity highs in either reef-building archaeocyathan or total animal species (Fig. 3). Although no significant total animal biodiversity high was associated with oxygenation pulse IV, the number of archaeocyathan species increased dramatically by ~60%. Moreover, the rising limb of isotope excursion IV coincided with the first emergence of trilobites, bivalved arthropods, and stenothecoids possessing relatively thick biomineralised skeletons, as well as a geographic expansion of possible burrowing filter-feeding arthropods over the Siberian Platform, as recorded by the appearance of *Thalassinoides*-type trace fossils[36]. A significant increase in the inter-habitat (beta)-diversity of reefal palaeocommunities was also restricted to the IV interval in the Aldan-Lena rivers region[2], reflecting a differentiation of species between assemblages, and thus ecological diversification within the shallow marine environment.

On a global scale, positive isotope excursion V appears to coincide with major radiations of large predatory arthropods and radiodonts, increased durophagy, and the first appearance of pelagic motile deuterostomes, evidenced by the Chengjiang biota and similar faunas[11,45]. Similarly, excursion VII coincided with a global radiation of echinoderms and archaeocyaths. The latter is revealed by the inter-regional (gamma)-diversity peak reflecting formation of numerous isolated faunal provinces[2]. By contrast, minor extinction events here and elsewhere appear to be associated with the negative excursions[11,18,46]. In the deeper ocean setting of northern Siberia and South China, multi-proxy analyses reveal broadly similar oceanic redox fluctuations[4,47–49], which coincide with the positive carbon isotope excursions in the early Cambrian[16,46,50]. These episodic redox oscillations, evident from the $\delta^{13}C$ record and, in places, as $\delta^{13}C$ and $\delta^{34}S$ covariance[16] (also see Supplementary Fig. S6 for $\delta^{13}C$-$\delta^{34}S$ covariance from the Cambrian Stage 2 ZHUjiaqing Carbon isotope Excursion (ZHUCE) in the Xiaotan section, South China), suggest that these coupled isotope excursions record a global phenomenon. We therefore propose that perturbations to shallow ocean oxygen budgets were driven by fluctuations in atmospheric oxygen. High oxygen levels would have suited various newly evolved animal body plans and lifestyles, and so oxygen fluctuations likely resulted in episodic expansions/contractions of the habitable zone within shallow ocean ecosystems. This shallow ocean oxygen control is likely reflected in contemporaneous fluctuations of animal origination and speciation rates, and thus possibly regulated the global radiation patterns of early Cambrian animals.

Expanded shallow ocean anoxia and sulphate reduction across the BTE

In contrast to the coupling of carbon and sulphur isotopes during Cambrian stages 2-3, the decoupled $\delta^{13}C$-$\delta^{34}S$ records and unsystematic temporal fluctuations in $\delta^{34}S$ values observed across the BTE (Fig. 1) appear to reflect a significant and persistent decline in oceanic sulphate concentration (Supplementary Fig. S2). At reduced marine residence times, $\delta^{34}S$ is more responsive to perturbations to the sulphur cycle. A fall in seawater sulphate concentration is generally attributed to enhanced evaporite deposition or widespread anoxia, and indeed, there are a number of thick evaporite deposits in the global rock record during this interval[51,52]. However, these evaporites are restricted to the innermost isolated basins of the Siberian Platform and the Australian part of Eastern Gondwana, and their stratigraphic distribution does not correlate with the interval of low sulphate inferred for the BTE. This suggests that anoxic/euxinic conditions likely prevailed in the shallow marine realm at this time. The expansion of shallow ocean anoxia is consistent with an observed accumulation of over ~750,000 km^2 of black organic-rich carbonate-rich sediments (comprising bituminous limestone, chert and argillaceous calcareous sapropelic shale) in the Sinsk Formation across the Siberian Platform, as well as enrichments in pyrite, V, As, Cr, Cu and Ni, and the presence of abundant biomarkers indicative of anaerobic bacteria as a major source of organic matter[21,53]. Such phenomena have previously been linked to shoaling of oxygen-depleted waters during a major marine transgression[21,36], which has been suggested as the cause of the major extinction pulse of the BTE (Sinsk event; Fig. 1). Thus, while bottom-water anoxia on the deeper portions of continental shelves and slopes may have contributed to the episodic burial of reductant and oxygenation of the atmosphere and shallow oceans in Cambrian stages 2-3, shoaling of anoxic waters in Cambrian Stage 4 may have driven a mass extinction, and therefore a reduction in primary productivity and overall reductant burial.

Implications for early animal diversification

Oxygenation of the early Cambrian shallow marine environment can be inferred from the coupled behaviour of the carbon and sulphur cycles. Episodic shallow ocean oxygenation corresponded to pulses of animal diversification, and so provides a plausible environmental explanation for the step-wise nature of the Cambrian radiation of animals. In the modern and ancient oceans, well-oxygenated waters are generally associated with larger body sizes, higher diversity, advanced skeletal biomineralization, and increased motility and carnivory[9,10,54,55]. Pulses of shallow ocean oxygenation in the early Cambrian likely expanded the global proportion of habitable marginal ocean to provide new ecological opportunities and biodiversity cradles. Similarly, the extended radiation of the Great Ordovician Biodiversification Event (~490–450 Ma) also appears to have been facilitated by pulses in atmospheric oxygenation[56]. A prolonged pause in biological diversification, which lasted over 20 million years and was associated with recurring extinctions (BTE, SPICE-trilobite extinctions[18]), occurred between these two major diversification events. Environmental stress caused by the persistent development of oxygen-deficient conditions in shallow marine realms due to low net atmospheric oxygen production[57] is likely to have been a major contributing factor. Thus, the global extent of well-oxygenated shallow ocean habitats during the early Paleozoic, as well as the maximum dissolved oxygen content of surface waters, played a vital role in regulating the emergence and radiation of early animal life.

References

1. Erwin, D. H. *et al.* The Cambrian Conundrum: Early Divergence and Later Ecological Success in the Early History of Animals. *Science.* **334**, 1091–1097 (2011).

2. Zhuravlev, A. Yu. & Naimark, E. B. Alpha, beta, or gamma: Numerical view on the Early Cambrian world. *Palaeogeogr. Palaeoclimatol. Palaeoecol.* **220**, 207–225 (2005).

3. Na, L. & Kiessling, W. Diversity partitioning during the Cambrian radiation. *Proc. Natl. Acad. Sci.* **112**, 4702-4706 (2015).

4. Boyle, R. A. *et al.* Stabilization of the coupled oxygen and phosphorus cycles by the evolution of bioturbation. *Nat. Geosci.* **7**, 671–676 (2014).

5. Lenton, T. M., Boyle, R. A., Poulton, S. W., Shields-Zhou, G. A. & Butterfield, N. J. Co-evolution of eukaryotes and ocean oxygenation in the Neoproterozoic era. *Nat. Geosci.* **7**, 257–265 (2014).

6. Chen, X. *et al.* Rise to modern levels of ocean oxygenation coincided with the Cambrian radiation of animals. *Nat. Commun.* **6**, 7142 (2015).

7. Mills, D. B. *et al.* Oxygen requirements of the earliest animals. *Proc. Natl. Acad. Sci.* **111**, 4168–4172 (2014).

8. Zhang, S. *et al.* Sufficient oxygen for animal respiration 1,400 million years ago. *Proc. Natl. Acad. Sci.* **113**, 1731–1736 (2016).

9. Sperling, E. A. *et al.* Oxygen, ecology, and the Cambrian radiation of animals. *Proc. Natl. Acad. Sci.* **110**, 13446–13451 (2013).

10. Levin, L. A., Gage, J. D., Martin, C. & Lamont, P. A. Macrobenthic community structure within and beneath the oxygen minimum zone, NW Arabian Sea. *Deep Sea Res. Part II Top. Stud. Oceanogr.* **47**, 189–226 (2000).

11. Zhu, M.-Y., Babcock, L. E. & Peng, S.-C. Advances in Cambrian stratigraphy and paleontology: Integrating correlation techniques, paleobiology, taphonomy and paleoenvironmental reconstruction. *Palaeoworld* **15**, 217–222 (2006).

12. Berner, R. A. GEOCARBSULF: A combined model for Phanerozoic atmospheric O_2 and CO_2. *Geochim. Cosmochim. Acta* **70**, 5653–5664 (2006).

13. Kump, L. R. & Garrels, R. M. Modeling atmospheric O_2 in the global sedimentary redox cycle. *Am. J. Sci.* **286**, 337–360 (1986).

14. Saltzman, M. R. *et al.* Pulse of atmospheric oxygen during the late Cambrian. *Proc. Natl. Acad. Sci.* **108**, 3876–3881 (2011).

15. Brasier, M. D., Corfield, R. M., Derry, L. A., Rozanov, A. Y. & Zhuravlev, A. Y. Multiple $\delta^{13}C$ excursions spanning the Cambrian explosion to the Botomian crisis in Siberia.

Geology **22**, 455 (1994).

16. Dahl, T. W. *et al.* Reorganisation of Earth's biogeochemical cycles briefly oxygenated the oceans 520 Myr ago. *Geochemical Perspect. Lett.* **3**, 210–220 (2017).

17. Maloof, A. C. *et al.* The earliest Cambrian record of animals and ocean geochemical change. *Geol. Soc. Am. Bull.* **122**, 1731–1774 (2010).

18. Peng, S., Babcock, L. E. & Cooper, R. A. The Cambrian Period. in *The Geologic Time Scale 2012* (eds. Gradstein, F. M., Ogg, J. G., Schmitz, M. D. & Ogg, G. M.) 437–488 (Elsevier Science Limited, 2012).

19. Tostevin, R. *et al.* Constraints on the late Ediacaran sulfur cycle from carbonate associated sulfate. *Precambrian Res.* **290**, 113–125 (2017).

20. Cui, H. *et al.* Redox-dependent distribution of early macro-organisms: Evidence from the terminal Ediacaran Khatyspyt Formation in Arctic Siberia. *Palaeogeogr. Palaeoclimatol. Palaeoecol.* **461**, 122–139 (2016).

21. Zhuravlev, A. Yu. & Wood, R. A. Anoxia as the cause of the mid-Early Cambrian (Botomian) extinction event. *Geology* **24**, 311 (1996).

22. Bambach, R. K. Phanerozoic Biodiversity Mass Extinctions. *Annu. Rev. Earth Planet. Sci.* **34**, 127–155 (2006).

23. Gill, B. C., Lyons, T. W. & Saltzman, M. R. Parallel, high-resolution carbon and sulfur isotope records of the evolving Paleozoic marine sulfur reservoir. *Palaeogeogr. Palaeoclimatol. Palaeoecol.* **256**, 156–173 (2007).

24. Veizer, J., Holser, W. & Wilgus, C. Correlation of $^{13}\mathrm{C}/^{12}\mathrm{C}$ and $^{34}\mathrm{S}/^{32}\mathrm{S}$ secular variations. *Geochim. Cosmochim. Acta* **44**, 579–587 (1980).

25. Algeo, T. J., Luo, G. M., Song, H. Y., Lyons, T. W. & Canfield, D. E. Reconstruction of secular variation in seawater sulfate concentrations. *Biogeosciences* **12**, 2131–2151 (2015).

26. Kah, L. C., Lyons, T. W. & Frank, T. D. Low marine sulphate and protracted oxygenation of the Proterozoic biosphere. *Nature* **431**, 834–838 (2004).

27. Brennan, S. T., Lowenstein, T. K. & Horita, J. Seawater chemistry and the advent of biocalcification. *Geology* **32**, 473 (2004).

28. Berner, R. A. Sedimentary pyrite formation: An update. *Geochim. Cosmochim. Acta* **48**, 605–615 (1984).

29. Gill, B. C. *et al.* Geochemical evidence for widespread euxinia in the Later Cambrian ocean. *Nature* **469**, 80–83 (2011).

30. Garrels, R. M. & Lerman, A. Coupling of the sedimentary sulfur and carbon cycles; an improved model. *Am. J. Sci.* **284**, 989–1007 (1984).

31. Bergman, N. M. COPSE: A new model of biogeochemical cycling over Phanerozoic time. *Am. J. Sci.* **304**, 397–437 (2004).

32. Algeo, T. J. & Ingall, E. Sedimentary C_{org}:P ratios, paleocean ventilation, and Phanerozoic atmospheric pO_2. *Palaeogeogr. Palaeoclimatol. Palaeoecol.* **256**, 130–155 (2007).

33. Handoh, I. C. & Lenton, T. M. Periodic mid-Cretaceous oceanic anoxic events linked by oscillations of the phosphorus and oxygen biogeochemical cycles. *Global Biogeochem. Cycles* **17**, 1–11 (2003).

34. Boulila, S. *et al.* On the origin of Cenozoic and Mesozoic "third-order" eustatic sequences. *Earth-Science Rev.* **109**, 94–112 (2011).

35. Haq, B. U. & Schutter, S. R. A Chronology of Paleozoic Sea-Level Changes. *Science.* **322**, 64–68 (2008).

36. Zhuravlev, A. Yu. Outlines of the Siberian platform sequence stratigraphy in the Lower and lower Middle Cambrian (Lena-Aldan area). *Rev. Española Paleontol.* 105–114 (1998).

37. Shields, G. A. & Mills, B. J. W. Tectonic controls on the long-term carbon isotope mass balance. *Proc. Natl. Acad. Sci.* **114**, 4318–4323 (2017).

38. Derry, L. A., Brasier, M. D., Corfield, R. M., Rozanov, A. Yu. & Zhuravlev, A. Yu. Sr and C isotopes in Lower Cambrian carbonates from the Siberian craton: A paleoenvironmental record during the 'Cambrian explosion'. *Earth Planet. Sci. Lett.* **128**, 671–681 (1994).

39. Feng, L., Li, C., Huang, J., Chang, H. & Chu, X. A sulfate control on marine mid-depth euxinia on the early Cambrian (ca. 529–521Ma) Yangtze platform, South China. *Precambrian Res.* **246**, 123–133 (2014).

40. Guilbaud, R. *et al.* Oxygen minimum zones in the early Cambrian ocean. *Geochemical Perspect. Lett.* **6,** 33–38 (2018).

41. Butterfield, N. J. Oxygen, animals and aquatic bioturbation: An updated account. *Geobiology* **16**, 3–16 (2018).

42. Jablonski, D., Sepkoski, J. J., Bottjer, D. J. & Sheehan, P. M. Onshore-Offshore Patterns in the Evolution of Phanerozoic Shelf Communities. *Science.* **222**, 1123–1125 (1983).

43. Zhuravlev, A. Yu. & Wood, R. A. The two phases of the Cambrian Explosion. *Sci. Rep.* **8**, 1–10 (2018).

44. Kiessling, W., Simpson, C. & Foote, M. Reefs as Cradles of Evolution and Sources of Biodiversity in the Phanerozoic. *Science.* **327**, 196–198 (2010).

45. Bicknell, R. D. C. & Paterson, J. R. Reappraising the early evidence of durophagy and drilling predation in the fossil record: implications for escalation and the Cambrian

Explosion. *Biol. Rev.* **93**, 754–784 (2018).

46. Wang, D. *et al.* Coupling of ocean redox and animal evolution during the Ediacaran-Cambrian transition. *Nat. Commun.* **9**, 2575 (2018).

47. Jin, C. *et al.* A highly redox-heterogeneous ocean in South China during the early Cambrian (~529–514 Ma): Implications for biota-environment co-evolution. *Earth Planet. Sci. Lett.* **441**, 38–51 (2016).

48. Zhang, J. *et al.* Heterogenous oceanic redox conditions through the Ediacaran-Cambrian boundary limited the metazoan zonation. *Sci. Rep.* **7**, 8550 (2017).

49. Zhang, L. *et al.* The link between metazoan diversity and paleo-oxygenation in the early Cambrian: An integrated palaeontological and geochemical record from the eastern Three Gorges Region of South China. *Palaeogeogr. Palaeoclimatol. Palaeoecol.* **495**, 24–41 (2018).

50. Wei, G.-Y. *et al.* Marine redox fluctuation as a potential trigger for the Cambrian explosion. *Geology* **46**, 1–5 (2018).

51. Kovalevych, V., Marshall, T., Peryt, T., Petrychenko, O. & Zhukova, S. Chemical composition of seawater in Neoproterozoic: Results of fluid inclusion study of halite from Salt Range (Pakistan) and Amadeus Basin (Australia). *Precambrian Res.* **144**, 39–51 (2006).

52. Astashkin, V. A. & Rozanov, A, I. Cambrian System on the Siberian Platform. Correlation chart and explanatory notes. *Int. Union Geol. Sci. Publ.* 1–133 (1991).

53. Parfenova, T. M., Korovnikov, I. V., Eder, V. G. & Melenevskii, V. N. Organic geochemistry of the Lower Cambrian Sinyaya Formation (northern slope of the Aldan anteclise). *Russ. Geol. Geophys.* **58**, 586–599 (2017).

54. Tostevin, R. *et al.* Low-oxygen waters limited habitable space for early animals. *Nat. Commun.* **7**, 12818 (2016).

55. Payne, J. L. *et al.* The evolutionary consequences of oxygenic photosynthesis: A body size perspective. *Photosynth. Res.* **107**, 37–57 (2011).

56. Edwards, C. T., Saltzman, M. R., Royer, D. L. & Fike, D. A. Oxygenation as a driver of the Great Ordovician Biodiversification Event. *Nat. Geosci.* **10**, 925–929 (2017).

57. Krause, A. J. *et al.* Stepwise oxygenation of the Paleozoic atmosphere. *Nat. Commun.* **9**, 4081 (2018).

Acknowledgements

This work was supported by the National Natural Science Foundation of China (41661134048) and Strategic Priority Research Program (B) of the Chinese Academy of Sciences (XDB18000000) to M.Z., NERC (NE/1005978/1 and NE/P013643/1) to G.A.S., University of Leeds Academic Fellowship to B.J.W.M., ERC Consolidator grant 682760 (CONTROLPASTCO2) to P.A.E.PvS, NERC (NE/N018559/1) to S.W.P., T.H. was supported by University College London Overseas Research Scholarship and the National Natural Science Foundation of China (41888101). We acknowledge G. Tarbuck and D. Hughes for assistance in the geochemical analysis. We thank T. W. Dahl, B. S. Wade, R. Newton, C. Yang and L. Yao for valuable discussions. We thank T. Algeo, B. Gill and M. Gomes for constructive comments.

Author contributions

T.H., M.Z., and G.A.S. conceived the project. G.A.S., P.A.E.PvS., B.J.W.M. and M.Z. supervised the project. M.Z., A.Y. and A.Yu.Z. collected the samples. T.H. and P.M.W. analysed the samples. A.Yu.Z. provided the fossil data. B.J.W.M. and T.H. created the models. All authors contributed to data interpretation and the writing of the manuscript.

Competing interests

The authors declare no competing interests.

Additional information

Correspondence and requests for materials should be addressed to T.H. (T.He@leeds.ac.uk)

Figure captions

Fig. 1. Carbonate carbon and carbonate-associated sulphate sulphur isotope records from Cambrian Stage 2 to Stage 4 of Siberian Aldan-Lena rivers sections. Regional stage subdivisions are shown next to the global subdivision plan for comparison[15] (F.: Fortunian Stage; N.–D.: Nemakit–Daldynian Stage; TST: Transgressive System Tract[36]; Fm.: Formation; A.: archaeocyaths; SSFs: small shelly fossils). Names for the positive $\delta^{13}C$ peaks (III, IV, V, VI, VII) are consistent with those of previously suggested $\delta^{13}C$ curves[15]. FAD: first appearance datum.

Fig. 2. Carbon and sulphur cycle model output. a. This model takes measured $\delta^{13}C$ values as an input parameter. **b**. Burial rates of organic carbon (C_{org}) are inferred from isotope mass balance and $\delta^{13}C$ record, and burial rates of pyrite are assumed to be controlled by modelled organic matter availability. **c**. Comparison between analysed $\delta^{34}S$ data (green curve) and simulated seawater sulphate $\delta^{34}S$ values (pink); Dashed part of the green curve shows the sampling gap. **d**. Variations in modelled net oxygen production. For all plots, the uncertainty window represents an alteration of the $\delta^{13}C$ values of carbon inputs between -5‰ and -8‰.

Fig. 3. Animal diversity, biological events and their correlation to the isotope records and oxygenation pattern across Cambrian stages 2-4. Global oxygen production is inferred from isotope mass balance modelling, using inputs of $\delta^{13}C$ only (light shade), or $\delta^{13}C$ and $\delta^{34}S$ (dark shade). Archaeocyathan species (blue line) and total animal species (green line) diversity records are expressed as the mean number of species per sampling unit (grey box) in Siberia; OP: oxygenation pulse; BH: biodiversity high; F.: Fortunian Stage; N.–D.: Nemakit–Daldynian Stage. FAD: first appearance datum.

Methods

Carbonate-associated sulphate (CAS) extraction and $\delta^{34}S$ analysis. Well preserved carbonate samples composed primarily of micrite were targeted for CAS extraction. Where that was not possible, few samples were selected with sparitic or dolomitic textures. Large blocks (>200 g) of carbonate rocks were cut and polished under running water to trim weathered surfaces prior to powdering. Blocks were then cut into small chips using a water-cooled, diamond tipped bench circular saw. Rock chips were ground to a fine powder (flour-like consistency, <10 µm) using a *Retsch*® Agate Mortar grinder. We applied a high-fidelity miniaturized CAS extraction protocol, which is an extension of two published approaches[58,59]. The protocol was established following tests involving twelve consecutive leaching steps on five carbonate samples from different stratigraphic horizons of the Aldan-Lena river sections and three samples from the Ediacaran Nama Group[19]. Approximately 10 g of the fine powder for each sample was leached in 40 ml of 10% NaCl solution for 24 hours to remove the non-CAS sulphur-bearing compounds and easily soluble sulphate. During leaching, samples were constantly agitated using a roller shaker at room temperature. Residues were rinsed in ultrapure water three times between each leach and five times after the final leach. After each leach, the leachate was retained, and the presence of sulphate was tested by adding saturated barium chloride solution and allowing three days to precipitate barite. As illustrated in Supplementary Fig. S3, the amount of sulphur removed during sequential NaCl leaching of test samples exhibited a sharp decline through multiple NaCl leaches and reached blank levels in the 3rd or 4th leachates, suggesting five leaches is sufficient for complete removal of all soluble sulphur-bearing constituents from ~10 g of carbonate powder. All five-times pre-leached carbonate samples were treated with 6 M HCl, which was added in calculated aliquots based on total HCl-leachable carbonate content. This step was completed within 30 minutes to minimise the potential for pyrite oxidation during dissolution. The insoluble residue was separated from the solution by centrifugation in 50 ml tubes followed by filtration through *VWR*® 0.2 µm Polypropylene membrane syringe filters. Saturated barium chloride solution was then added to the filtered solution and left to precipitate within the housing of a sealed tube over three days at room temperature. Where no visible precipitate was observed after 24 h, 2 mg isotopic-grade sulphur-free quartz powder was added, which served as an inert medium onto which barium sulphate could precipitate[59]. Each sample was centrifuged, and the supernatant replaced with ultrapure water repeatedly until the pH attained neutral values. Washed samples were then dried prior to isotope analysis. $^{34}S/^{32}S$ analysis of barium sulphate precipitates was undertaken using an *Elementar*® Pyrocube elemental analyzer linked to an *Isoprime*® 100 mass spectrometer operated in continuous flow mode at the Lancaster Environment Centre, Lancaster University. Pellets of $BaSO_4$, resulting from sulphate extraction with or without the addition of quartz powder, were combusted in tin capsules in the presence of excess vanadium pentoxide (V_2O_5) at 1030°C to yield SO_2 for the determination of $\delta^{34}S$. All samples and standards were matrix matched, and values were corrected against VCDT using within-run analyses of international standards NBS-127 and SO5 (assuming $\delta^{34}S$ values of +20.3‰ and +0.49‰, respectively). Within-run standard replication was below 0.3‰ (1sd). Procedural standard solutions of calcium sulphate precipitated as barium sulphate were used to test the integrity of the method[59]. These yielded $\delta^{34}S$ values of +2.7‰ (±0.3‰, 1sd, n=12) compared to values of +3.0‰ (±0.3‰, 1sd, n=13) for analysis of the raw calcium sulphate powder. Blank contamination associated with $\delta^{34}S$ determination was zero.

CAS concentrations and sulphur content in NaCl leached solution.

The concentration of CAS and sulphur content in each leaching step was measured in aliquots of filtered solution using a *Varian*® 720 Inductively Coupled Plasma Optical Emission Spectrometer (ICP-OES) at the London Geochemistry and Isotope Centre (LOGIC), University College London. Wavelength 182.5 nm was selected to minimise interference with calcium ions, and analysis was conducted using the N_2-purging polyboost function to avoid oxygen interference in the system.

Carbonate carbon and oxygen isotopes. Micritic limestone was targeted for $\delta^{13}C$ analysis. Where that was not possible, we selected a few sparitic or dolomitised samples and fossiliferous samples with skeletal components known to secrete low-Mg calcite. About 20 mg of powder drilled from a rock chip was analyzed for stable C and O isotopes. Limestone samples were reacted with 100% H_3PO_4 at 25°C for more than 12 h, and dolostone samples were reacted with 100% H_3PO_4 at 50°C for more than 24 h. Prepared gas samples were analysed for $^{13}C/^{12}C$ and $^{18}O/^{16}O$ using the Chinese national standard, an Ordovician carbonate from a site near Beijing (reference number GBW04405: $\delta^{13}C$= 0.57 ± 0.03‰ VPDB;

$\delta^{18}O$= -8.49 ± 0.13‰ VPDB). The analyses were performed using the *Finnigan*® MAT 253 mass spectrometers at the Nanjing Institute of Geology and Palaeontology, Chinese Academy of Sciences.

Elemental analysis. For concentrations of diagenesis-diagnostic elements, including Ca, Mg, Mn, and Sr, an aliquot of approximately 50 mg of power was micro-drilled from a rock chip and dissolved with excess 6 M hydrochloric acid at room temperature for 12 h. The concentration of acid used here is identical to the concentration used during CAS extraction. The reaction was facilitated using an ultrasonic bath and roller shaker. After centrifugation, aliquots of the supernatant were analysed for elemental concentration using a *Varian*® 720 ICP-OES at University College London. Solution standards of certified reference materials, SRM1c (argillaceous limestone) and SRM120b (Florida phosphate rock), were run at the start of the analyses along with a blank to monitor the accuracy of the bulk elemental analysis. Laboratory control solution standards were also run after every batch of 20 samples to monitor drift and precision. Analytical precision for elemental concentrations was generally better than 5%.

'Rate method' model. Maximum seawater sulphate concentrations are calculated using the modified 'rate method'[25,26]. The model was constructed based on the observed rate of change in seawater sulphate (carbonate-associated sulphate) $\delta^{34}S$, fractionation between oxidized (sulphate) and reduced sulphur (pyrite) reservoirs and equation (1) that connects the two parameters, where F_x represents the input and output fluxes, $\Delta^{34}S_x$ represents isotopic difference of $\delta^{34}S$ values between fluxes (Q = total input flux of sulphur, SUL = seawater sulphate, PY = pyrite burial, SW = seawater/sulphate deposition) and M_{SW} represents the mass of sulphate in the ocean.

$$\frac{d\delta^{34}S}{dt} = \frac{\left(\left(F_Q \times \Delta^{34}S_{Q-SW}\right) - \left(F_{PY} \times \Delta^{34}S_{SUL-PY}\right)\right)}{M_{SW}} \qquad (1)$$

The maximum rates of $\delta^{34}S$ change are attained when sulphur input flux to the ocean approaches zero (F_Q = 0), and the standing oceanic sulphate reservoir is removed as pyrite. Equation (1) is then transformed to equation (2) to calculate the size of seawater sulphate reservoir.

$$M_{SW} = \frac{F_{PY} \times \Delta^{34}S_{SUL-PY}}{\frac{d\delta^{34}S}{dt}} \qquad (2)$$

Because the observed rates of seawater sulphate δ^{34}S change in a normal marine environment should never exceed the theoretical maximum rates of change ($d\delta^{34}$S/dt), the calculation of M_{SW} using equation (2) should provide the maximum estimate of seawater sulphate concentration. The definition of F_{PY}, $\Delta^{34}S_{SUL-PY}$, and unit-conversion constants (gram to mM) are consistent with the values applied for the long-term secular variation of seawater sulphate concentration[25]. $F_{PY} = 4 \times 10^{13}$ g yr^{-1} is suggested for a normal marine environment. $\Delta^{34}S_{SUL-PY}$ = 35‰ is suggested for the fractionation during MSR. The variation of seawater sulphate concentration ([SO_4^{2-}]) between ~524 Myr ago and ~512 Myr ago is represented based on a point-to-point calculation (Supplementary Fig. S2). Because the sampling density between δ^{34}S values is generally below 0.1 Myr (Supplementary Table S3), this study uses a 0.1 Myr gridded data smoothing curve (red line in Supplementary Fig. S2) to represent the best estimate of seawater [SO_4^{2-}]. Besides, the maximum concentration for an individual point could be under or overestimated due to fluctuations and anomalies in the rate of δ^{34}S changes. To overcome this bias, the resulting [SO_4^{2-}] data are binned into 0.5 Myr bands. The lower envelope (black dotted line in Supplementary Fig. S2) of the [SO_4^{2-}] red curve, which links the lowest value for each band, is expected to represent the maximum rates of δ^{34}S change and thus the theoretical estimate of maximum seawater sulphate concentration through time.

Coupled carbon and sulphur cycle model. A simple model of the global carbon and sulphur cycles was applied to explore the proposed mechanisms for isotopic variations in the system. This follows the work of Garrels and Lerman[30], Berner[12] and Bergman *et al.*[31]. The model calculates the global rate of organic carbon burial using isotope mass balance, and then attempts to predict the operation of the sulphur system based on the supply of organic matter. Supplementary Fig. S4 shows the model processes as a diagram; Supplementary Table S2 shows the model flux and parameter values. The model estimates long-term fluxes between the ocean and sediments for both carbon and sulphur. Carbon is modelled as CO_2 in the atmosphere and ocean (A), and will be buried either as organic carbon (G) or carbonate (C). Similarly, sulphur can exist as oceanic sulphate (S), and will be buried as pyrite (PYR) or gypsum (GYP). Weathering (and metamorphism) constitutes the return flux from the sediments to the ocean and atmosphere. We set the weathering inputs to constant values in line with previous models[12,31]. We allow for around half of present total organic carbon burial (and weathering) due to the absence of land plants, and an enhanced burial flux of pyrite sulphur due to anoxia. The weathering rate of gypsum is held constant, but the burial rate is adjusted so that the model maintains a constant sulphate concentration. Due to the relatively short model timeframe relative to the residence times of the vast sedimentary reservoirs, these reservoirs are assumed to have a fixed isotopic composition and are assumed not to vary in size. The ocean and atmosphere reservoirs are allowed to vary in size and isotopic composition. Organic carbon burial is calculated via isotope mass balance[12,30], which uses the total carbon input fluxes and isotopic composition of seawater (δA) to calculate the required burial rate of isotopically depleted organic carbon (equation (3)):

$$B(G) = \frac{1}{\Delta B}\{\, W(G)(\delta A - \delta G) + W(C)(\delta A - \delta C)\} \tag{3}$$

It is assumed that pyrite burial is governed by the supply rate of organic carbon to microbial sulphate reducers, and therefore scales with the burial rate of organic carbon (equation (4)). The proportionality constant (0.5) is chosen to balance pyrite weathering.

$$B(PYR) = 0.5\,B(G) \tag{4}$$

Variation in the ocean and atmosphere carbon is calculated as:

$$\frac{dA}{dt} = W(G) + W(C) - B(G) - B(C) \tag{5}$$

Variation in ocean sulphate is calculated as:

$$\frac{dS}{dt} = W(PYR) + W(GYP) - B(PYR) - B(GYP) \tag{6}$$

Variation in the isotopic composition of ocean sulphate is calculated as:

$$\frac{d(S \times \delta S)}{dt} = W(PYR)\delta PYR + W(GYP)\delta GYP - B(PYR)(\delta S - \Delta S) \\ - B(GYP)\delta S \tag{7}$$

Net oxygen production flux is calculated from the burial rate of organic carbon and pyrite:

$$FO_2 = B(G) + 2 \cdot B(PYR) \tag{8}$$

The model is solved in MATLAB using the ODE (Ordinary Differential Equation) suite. The model broadly reproduces the duration and magnitude of fluctuations in δ^{34}S (Fig. 2c). It also predicts similar fluctuations in oxygen production (Fig. 2d). The model does not calculate the concentration of oxygen in the atmosphere and ocean, and all fluxes are assumed to be oxygen-independent. More detailed modelling, which takes into account the variation in oxygen sinks, is required to analyse the overall long-term trends in atmospheric oxygen levels.

An alternative version of the model is run in Fig. 3 that estimates pyrite burial rates directly from the $\delta^{34}S$ record. In this version, equation (4) is replaced by equation (9), and equation (7) is not required.

$$B(PYR) = \frac{1}{\Delta S}\{ W(PYR)(\delta S - \delta PYR) + W(GYP)(\delta S - \delta GYP)\} \qquad (9)$$

Total marine animal species diversity. Supplementary Table S4 shows the distribution and diversity of total and individual animal species of Cambrian stages 2-4 of the Siberian Platform. This dataset is an upgrade of a previously published version[21] (see supplementary information for detailed description and source of data). Siberian biozones (archaeocyathids/trilobite) are selected as the sampling units for diversity data collection. The finalised animal diversity record is generated by plotting total species diversity against sampling units (grey boxes in Fig. 3).

Code availability.

The code used to generate the Coupled carbon and sulphur cycle model results is available from the corresponding author (T.He@leeds.ac.uk) on request.

Data availability.

The authors declare that data supporting the findings of this study are available within the article and Supplementary Tables S1–S5.

References

58. Wotte, T., Shields-Zhou, G. A. & Strauss, H. Carbonate-associated sulfate: Experimental comparisons of common extraction methods and recommendations toward a standard analytical protocol. *Chem. Geol.* **326–327,** 132–144 (2012).

59. Wynn, P. M., Fairchild, I. J., Baker, A., Baldini, J. U. L. & McDermott, F. Isotopic archives of sulphate in speleothems. *Geochim. Cosmochim. Acta* **72,** 2465–2477 (2008).

Figure 1

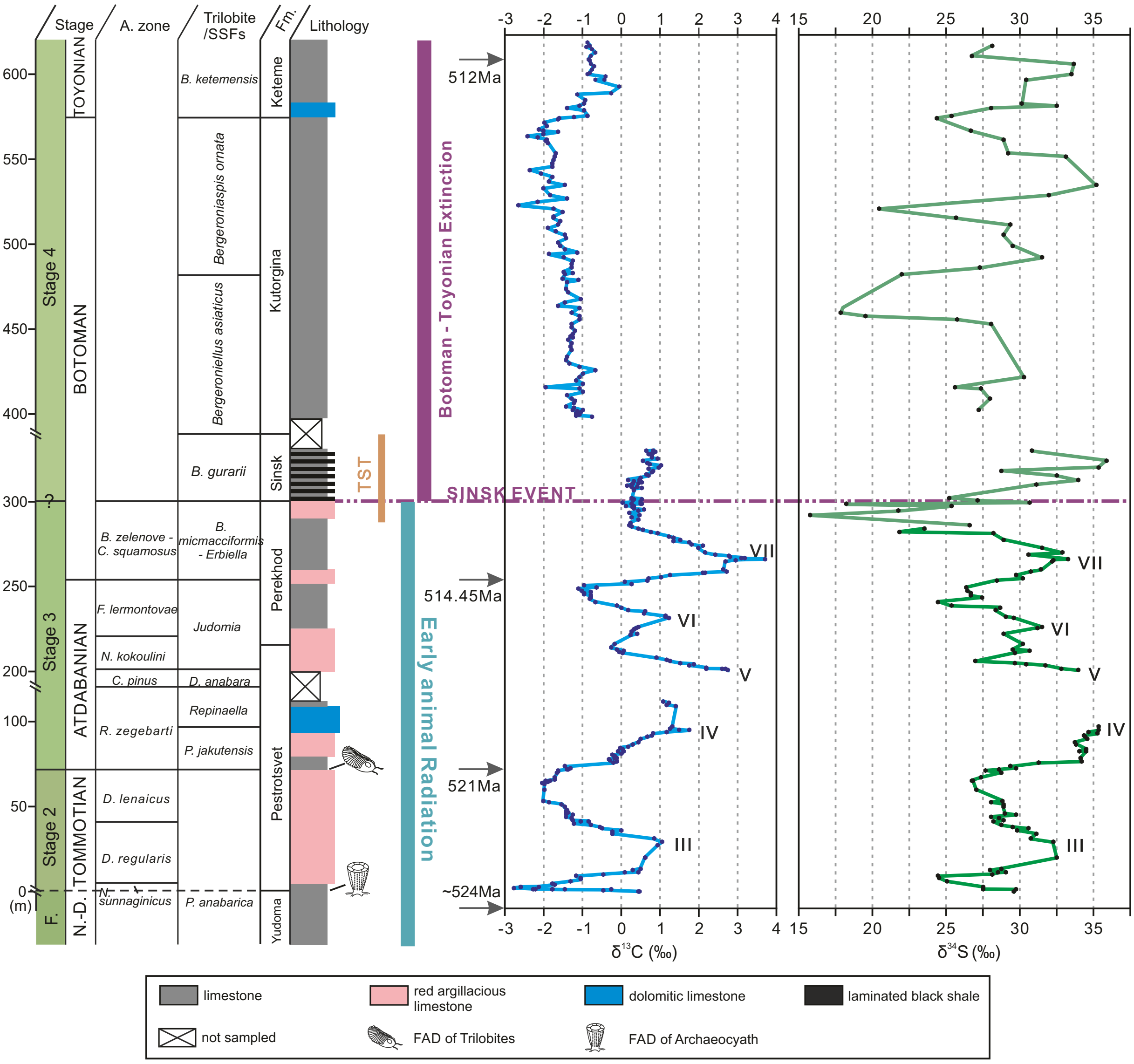

Stage
A. zone
Trilobite /SSFs
Fm.
Lithology
600
550
500
450
400
300
250
200
100
50
0
(m)
Stage 4
?
Stage 3
Stage 2
F.
TOYONIAN
BOTOMAN
ATDABANIAN
TOMMOTIAN
N.-D.
B. zelenove - C. squamosus
F. lermontovae
N. kokoulini
C. pinus
R. zegebarti
D. lenaicus
D. regularis
N. sunnaginicus
B. ketemensis
Bergeroniaspis ornata
Bergeroniellus asiaticus
B. gurarii
B. micmacciformis - Erbiella
Judomia
D. anabara
Repinaella
P. jakutensis
P. anabarica
Keteme
Kutorgina
Sinsk
Perekhod
Pestrotsvet
Yudoma
TST
Botoman - Toyonian Extinction
Early animal Radiation
SINSK EVENT
512Ma
514.45Ma
521Ma
~524Ma
-3
-2
-1
0
1
2
3
4
VII
VI
V
IV
III
δ13C (‰)
15
20
25
30
35
δ34S (‰)
limestone
red argillacious limestone
dolomitic limestone
laminated black shale
not sampled
FAD of Trilobites
FAD of Archaeocyath

Figure 2

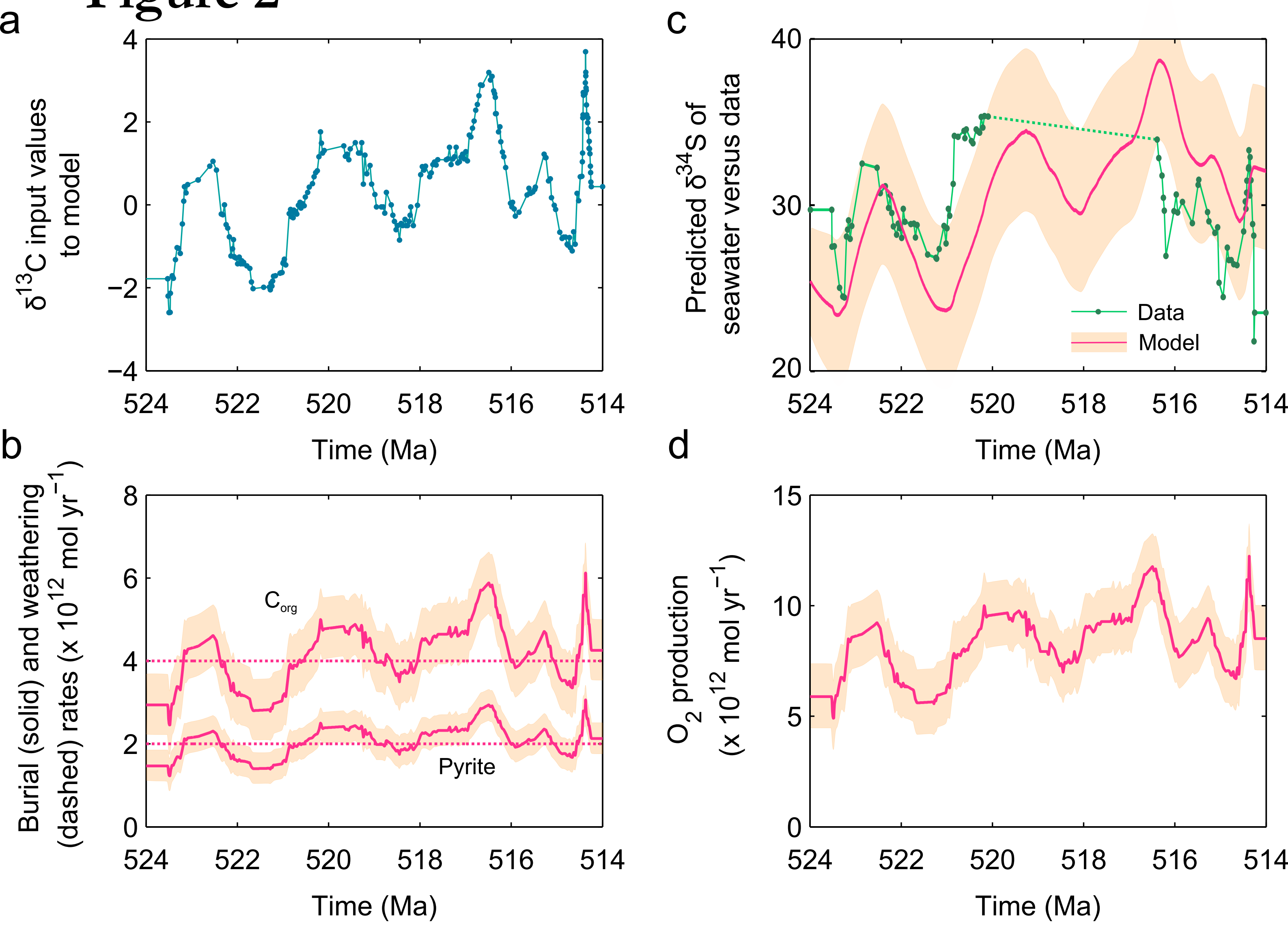
a
δ13C input values to model
4
2
0
−2
−4
524
522
520
518
516
514
Time (Ma)
b
Burial (solid) and weathering (dashed) rates (x 10^12 mol yr^−1)
8
6
4
2
0
Corg
Pyrite
524
522
520
518
516
514
Time (Ma)
c
Predicted δ34S of seawater versus data
40
30
20
Data
Model
524
522
520
518
516
514
Time (Ma)
d
O2 production (x 10^12 mol yr^−1)
15
10
5
0
524
522
520
518
516
514
Time (Ma)

Figure 3

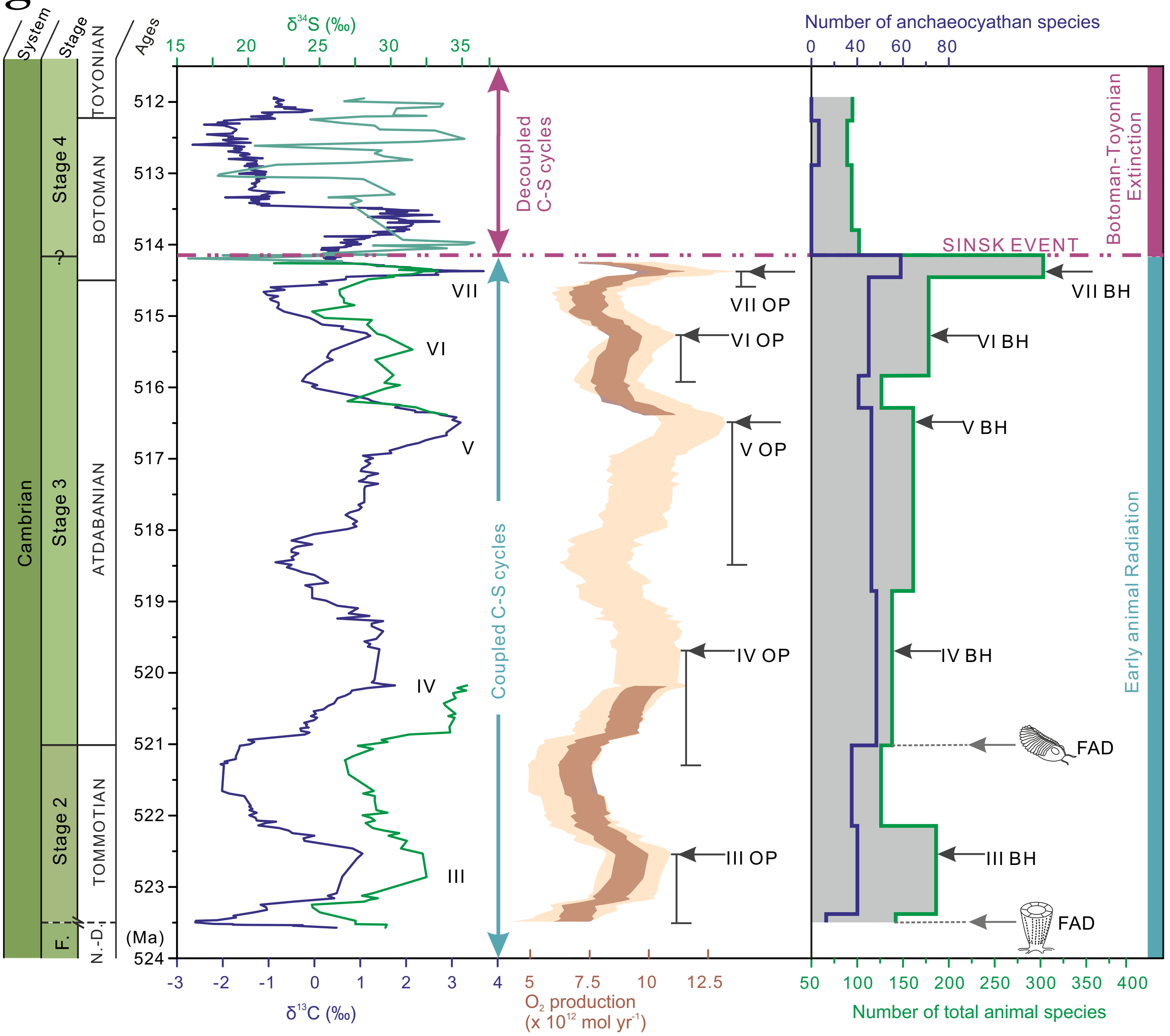
System
Stage
Ages
Cambrian
Stage 4
Stage 3
Stage 2
F.
?
TOYONIAN
BOTOMAN
ATDABANIAN
TOMMOTIAN
N.-D.
512
513
514
515
516
517
518
519
520
521
522
523
524
(Ma)
δ34S (‰)
15
20
25
30
35
δ13C (‰)
-3
-2
-1
0
1
2
3
4
VII
VI
V
IV
III
Decoupled C-S cycles
Coupled C-S cycles
O2 production (x 10^12 mol yr^-1)
5
7.5
10
12.5
VII OP
VI OP
V OP
IV OP
III OP
SINSK EVENT
Number of anchaeocyathan species
0
40
60
80
Number of total animal species
50
100
150
200
250
300
350
400
VII BH
VI BH
V BH
IV BH
III BH
FAD
FAD
Botoman-Toyonian Extinction
Early animal Radiation

Supplementary information for

Possible links between extreme oxygen perturbations and the Cambrian radiation of animals

Tianchen He*, Maoyan Zhu, Benjamin J.W. Mills, Peter M. Wynn, Andrey Yu. Zhuravlev, Rosalie Tostevin, Philip A. E. Pogge von Strandmann, Aihua Yang, Simon W. Poulton, Graham A. Shields

*Correspondence and requests for materials should be addressed to T.H. (T.He@leeds.ac.uk)

SI Guide:

- Supplementary Notes
- Supplementary Figs. S1 to S7
- Supplementary Tables S1 and S2
- Captions for Supplementary Tables S3 to S5
- Supplementary References

Additional supplementary files (separate files):

- Supplementary Table S3 (Excel file)
- Supplementary Table S4 (Excel file)
- Supplementary Table S5 (Excel file)

Supplementary Notes:

Geology, stratigraphic, lithological, palaeontological context, and samples. The type sections of the lower Cambrian subdivisions and their lower boundaries are located in the south-eastern part of the Siberian Platform. The main sections are outcrop along the Aldan and Lena rivers (Supplementary Fig. S1) and are suggested to have formed in a normal-salinity, shallow, open marine environment[1]. Samples were collected from seven lower Cambrian carbonate-dominated sections along the Aldan and Lena rivers, and in ascending Siberian Stage stratigraphic order include Dvortsy, Isit', Zhurinsky Mys, Ulakhan-Kyyry-Taas, Ulakhan-Tuoidakh, Labaia and Tit-Ary sections. These sections are the stratotype sections for the lower Cambrian chronostratigraphic units used in Russia, and the total thickness of the sequences is ~600 m, spanning the Cambrian Stage 2 to Stage 4 interval. Importantly, the GSSPs of the Cambrian stages 2–4 are not determined, but the provisional international subdivision is largely based on the fossil distribution and stages established in these Siberian sections. Moreover, since the Aldan-Lena rivers sections are unique with respect to archaeocyath, trilobite, and other fossils abundances, and many of these forms were found from all over the world, these subdivisions are globally recognised. The investigated sedimentological sequence is represented mainly by micritic/sparitic limestones with well-preserved skeletal (exclusively benthic), ooid, marine cement fabrics[2–6] and only a few dolomitic beds. Nearly 400 well-preserved carbonate samples were systematically collected following the regional stratigraphic guidebook for the lower Cambrian subdivision of the Siberian Platform[1], with a sampling resolution of roughly 50 cm to 1 m spacing. 352 well-preserved carbonates were analysed for carbon and oxygen isotopes; 142 samples were analysed for carbonate-associated sulphate (CAS) sulphur isotopes, concentrations of diagenetic-diagnostic elements, and [CAS].

Age model. Carbon isotope results shown in Supplementary Table S3 and Fig. 1 confirm the long-term $\delta^{13}C$ trend, values and amplitudes of all short-term carbon-isotope oscillations presented in previous studies on the Siberian Platform[4,7,8]. The current study recovered three full carbonate $\delta^{13}C_{carb}$ positive excursions (III, VI, VII), the rising limb of IV and the falling limb of V. These sections are finely subdivided by both archaeocyath and trilobite zones which are globally correlated. An age model consistent with the internationally agreed numerical time scale[9] is applied to the studied sections. The stratigraphically calibrated age for the base of Series 2 (= base Stage 3) was suggested to be ~521 Ma[9], and is the age tie point for the FAD of trilobites (base of the *Profallotaspis jakutensis* Trilobite Zone and of the Atdabanian Stage) on the Siberian Platform. This estimate derives largely from a radiometrically determined age of 520.93±0.4 Ma, which can be tied to the basal part of positive carbon isotope excursion IV in Morocco[10,11] and Siberian Aldan-Lena rivers sections (Fig. 1). A volcanic ash bed in Shropshire, England yields an U–Pb zircon age for the middle *Callavia* Trilobite Zone of 514.45±0.36 Ma[12] and provides an estimate for the age of the uppermost Atdabanian *Fansycyathus lermontovae* Archaeocyath Zone on the Siberian Platform[11,13]. The well-known early Cambrian Konservat-Lagerstätte – South China Chengjiang biota (Maotianshan Shale Member, Yu'anshan Formation) – is correlated with the interval from the *Delgadella anabara* Zone to lower *Judomia* Zone in Siberia[9]. The Chengjiang biota is assigned an age of ~516–517 Ma based on the age model in the current study, which is consistent with the recently reported numerical age, based on detrital zircon U–Pb analyses, which constrain the Chengjiang biota to no older than 518.03 Ma[14]. Accordingly, the Sirius Passet Lagerstätte is correlated with the Laurentian *Esmeraldina rowei* Trilobite Zone, approximately corresponding to the upper *Judomia* Trilobite Zone in Siberia[15] and assigned an age of ~514.5–515 Ma in the current age model. In addition, U–Pb zircon analyses for the middle *Callavia* Trilobite Zone constrain the age of the basal Botoman (Stage 4) *Bergeroniellus micmacciformis* – *Erbiella* Trilobite Zone to be 514 Ma. Ash beds of 511±1.0 Ma and 509.1±0.22 Ma occur in strata bearing fossils from the *Geyerorodes howleyi* and *Acadoparadaxides harlani* trilobite zones of the former Avalon continent, which encompasses eastern Newfoundland, the southern British Isles and some other areas[12,16], and thus brackets the Toyonian/Amgan (Series 2/3) boundary in Siberia at ~510 Ma[17]. A constant sediment accumulation rate (0.007 Myr/m) is assumed between the *Lermontovia grandis* Trilobite Zone, which is time equivalent with the *Geyerorodes howleyi* Zone (~511 Ma), and the lowermost Botoman *Bergeroniellus micmacciformis – Erbiella Zone* (514.45 Ma) in Fig. 1 based on current and previously reported stratigraphic thickness in between[4]. Based on the calculation, an age of ~512 Ma is suggested for the topmost stratigraphic horizon (middle *Bergeroniellus ketemensis* Zone) as shown in Fig. 1. Therefore, three age tie points including 512 Ma, 514.45 Ma, and 521 Ma are applied to the studied stratigraphy (Supplementary Table S3 and Fig. 1). The age assignment for each sample assumes constant sediment accumulation rates between age tie points. The full age framework and its correlation with archaeocyath, trilobite, and small shelly fossil biozones are shown in Supplementary Table S3.

Source of biodiversity data. The Alden-Lena Rivers carbonate platform represents a unique setting for the preservation of early Cambrian marine animal biodiversity – of the c. 2000 recorded early Cambrian genera, 350 were described for the first time at this site, and over half of all known global biodiversity is represented on this platform[1,13,18]. Biodiversity data have been collated at the species level (e.g. beta-diversity of reefal palaeocommunities) for the Siberian platform and at the genus level globally[4,6,13]. A new part of this compilation and basic sources are reported in Zhuravlev and Wood (2018), omitting synonyms and poorly identified forms[19]. The majority of these biodiversity data were obtained from the same reference sections as samples for C- and S-isotope analyses in the current study. Data collected from other sections can be clearly correlated to the Aldan-Lena Rivers sections through visual tracing of individual lithological beds within the Siberian platform. Indeed, the beta-diversity data for reefal palaeocommunities were obtained from the exact same reference section[20].

Evaluating diagenesis. It is important to constrain the degree to which bulk carbonate or skeletal components (both low-Mg calcite) have been altered to establish whether geochemical trends are likely to be representative of syndepositional oceanic values. Interaction with diagenetic fluids (e.g. meteoric, burial fluids) during dissolution and recrystallisation of shallow marine carbonates can simultaneously lower the $\delta^{13}C$ and $\delta^{18}O$ values in carbonate rocks[21–24]. Therefore, a positive correlation between $\delta^{13}C$ and $\delta^{18}O$ is often considered to be a tentative indicator of diagenetic alteration. As shown in Supplementary Fig. S5, $\delta^{13}C$ v. $\delta^{18}O$ cross-plots for the Aldan-Lena river sections exhibit only weak positive correlation ($R^2 = 0.213$). Although this trends to support only minor diagenetic overprinting, we note that non-diagenetic covariations can arise even in seemingly primary trends, such as in the long-term Ordovician $\delta^{13}C$ and $\delta^{18}O$ record[25]. More convincingly, the $\delta^{13}C$ records shown in Fig. 1 exhibit a gradual and extremely smooth curve through Cambrian stages 2-4, and both the long-term trends and magnitudes of short-term $\delta^{13}C$ excursions are globally identical[9,26], which is a robust indication of its primary nature. Furthermore, previous study of materials at Siberian Aldan-Lena rivers sections also shows that $\delta^{13}C$ values exhibit isotopic consistency between skeletal fabrics, primary marine cement and micrite analysed from the same carbonate rock[4]. Therefore, $\delta^{13}C$ and $\delta^{18}O$ systematics of the Aldan-Lena rivers sections are likely to represent primary isotopic signatures of coeval seawater rather than alteration during diagenesis.

Carbonate associated sulphate (CAS), whereby marine sulfate is structurally substituted into the carbonate lattice, is considered to be a robust proxy archive that records syndepositional seawater sulphate, if CAS $\delta^{34}S$ values and concentration have not been impacted by diagenetic overprinting[27–29]. Previous work has shown that CAS content decreases in carbonates as they undergo exchange with burial fluids at increasing degrees of burial depth and temperature[29–31]. Despite changes in CAS concentrations, no significant variations in the CAS sulphur isotopic composition were found during progressive burial diagenesis[29,32]. These results suggest that CAS $\delta^{34}S$ values are resistant to late stage burial alteration, but analysed CAS concentration from a bulk carbonate may not be considered a reliable indicator of original seawater sulphate levels. CAS contents in this study are consistently high (majority > 100 ppm), and exhibit no correlation with $\delta^{34}S$ ($R^2 = 0.025$) (Supplementary Fig. S5). Post-depositional dolomitisation also has the potential to influence $\delta^{34}S$ values of CAS[33] and simultaneously alter carbonate $\delta^{18}O$ values[34], but dolomitic samples were avoided during sampling, and no correlation is seen between $\delta^{34}S$ values and Mg/Ca ($R^2 = 0.003$) or $\delta^{18}O$ ($R^2 = 0.008$) (Supplementary Fig. S5), indicating that $\delta^{34}S$ values do not vary due to partial dolomitisation.

Early diagenetic exchange with pore fluids can also produce changes in the isotopic composition and abundance of CAS. For example, sulphate reduction in anoxic pore waters causes progressive enrichment of ^{34}S in the residual sulphate pool, in tandem with a decline in sulfate concentrations. During carbonate burial, if neomorphism of primary aragonitic phases to calcite occurs in a critical interval where sulphate is abundant, but also isotopically enriched, CAS may be altered towards elevated $\delta^{34}S$[31,35]. Variability in CAS $\delta^{34}S$ values may be present between different sedimentary components in bulk carbonate rocks[36]. Our samples show no obvious evidence for recrystallisation from an earlier aragonitic phase, but do include a mixture of calcified fossils with micritic and sparitic textures in a few samples from the interval with coupled $\delta^{13}C$-$\delta^{34}S$ cycles (Supplementary Fig. S7). However, no correlations are observed between δ^{34}S values and HCl-leachable carbonate content ($R^2 = 0.002$) or Mg/Ca ($R^2 = 0.003$) (Supplementary Fig. S5), suggesting that variability in lithology or carbonate phases did not exert a diagenetic control over the variations in CAS δ^{34}S records. The current δ^{34}S record may derive from an integrated signal of homogenized bulk rock carbonate associated sulphate that is close to the coeval seawater. Also, cross-plots of CAS δ^{34}S values show no correlation with traditional indicators of diagenesis, including CAS concentration ($R^2 = 0.025$), Mn/Sr ($R^2 < 0.0001$) or δ^{18}O ($R^2 = 0.008$) (Supplementary Fig. S5), suggesting that the samples could potentially preserve primary seawater sulphate δ^{34}S values.

CAS may be contaminated by either the oxidation of pyrite or present-day secondary atmospheric sulphate (SAS) during the chemical extraction[33,37]. Our analysed samples are generally low in petrographically visible pyrite (except for carbonates of Sinsk Formation) and precautions were taken to minimise the potential for pyrite oxidation during carbonate acid dissolution (see Methods). Present-day SAS should only be incorporated into the bulk carbonate rock at leachable sites via weathering, and would generally not affect the primary calcite lattices where CAS is located. The current study applied multiple consecutive NaCl pre-leaches, which demonstrate the elimination of soluble sulphate contaminants (see Methods), therefore minimising potential SAS contamination. Finally, the observed δ^{34}S trend and excursions (Fig. 1) show an extremely smooth curve with minor scatter, likely resulting from variability in primary isotopic signature in the early Cambrian seawater sulphate, rather than variable diagenetic overprinting or experimental contamination.

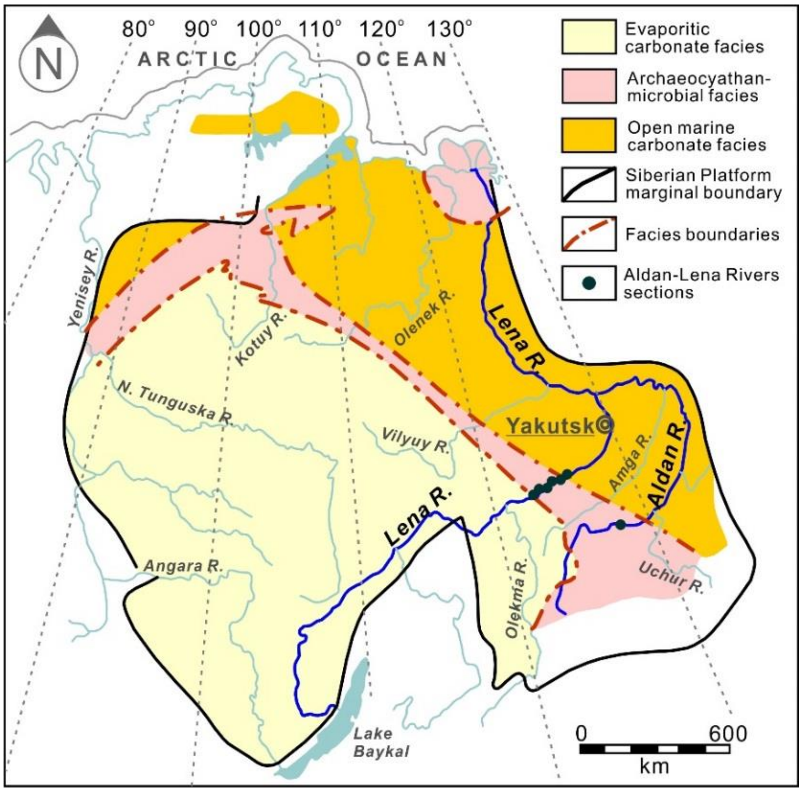

Supplementary Fig. S1. Simplified geological map of the Siberian Platform during the early Cambrian. The map shows modern rivers, major sedimentary facies basins and localities of studied sections. R.: river.

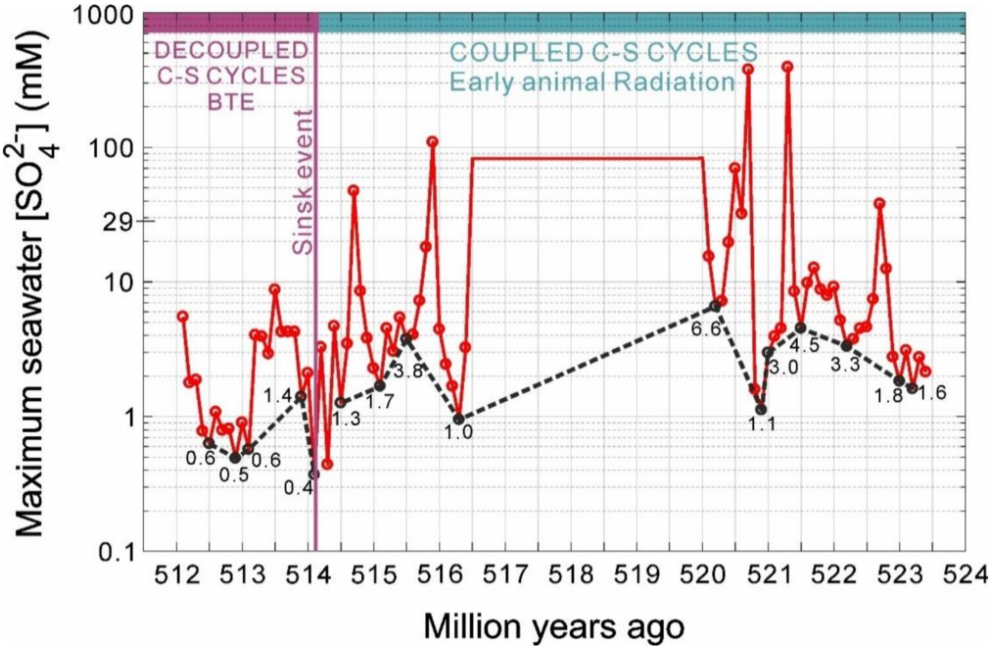

Supplementary Fig. S2. Secular variation of maximum seawater sulphate concentration [SO_4^{2-}] from Cambrian Stage 2 to Stage 4 (~524-512 Ma) for the southeastern Siberian platform. The resulting red curve exhibits variations in maximum seawater [SO_4^{2-}] with data smoothing grids at 0.1 Myr (red). The black dotted line represents the lower end of the data envelope and the best estimate of variation in sulphate concentration. [SO_4^{2-}] values are marked next to the black dotted data points representing the lowest values for the 0.5 Myr bands. Coupled C-S cycles: interval of animal radiation when $\delta^{13}C$ and $\delta^{34}S$ records are positively correlated; Decoupled C-S cycles: interval when $\delta^{13}C$ and $\delta^{34}S$ records are decoupled. BTE: Botoman–Toyonian Extinction.

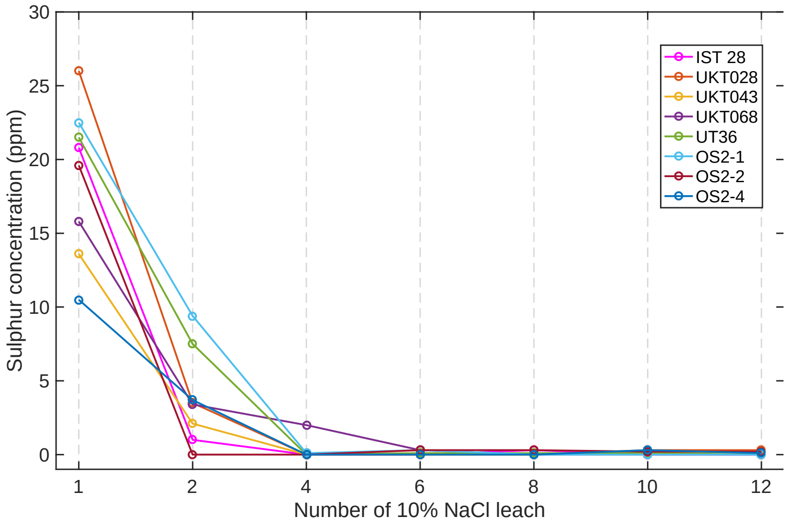

Supplementary Fig. S3. Sulphur concentration variations in 10% sodium chloride-leached solution from different stages of multiple leaching (leach 1, 2, 4, 6, 8, 10, 12). Test samples IST28, UKT028, UKT043, UKT068, UT36 are Cambrian carbonate from the Siberian Aldan-Lena rivers sections. OS2-1, OS2-2, OS2-4 are test samples of marine carbonate from the Ediacaran Nama Group, Namibia.

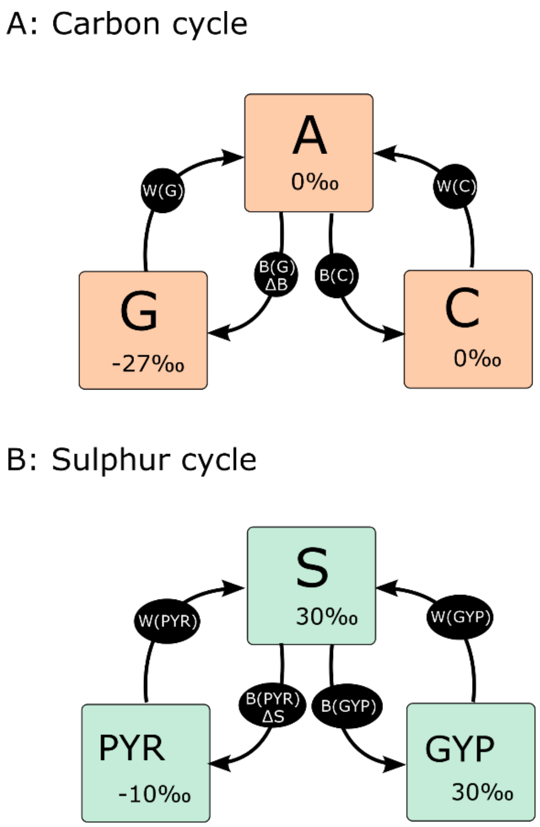

Supplementary Fig. S4. Coupled C-S cycle model diagram. Boxes show reservoirs and arrows show fluxes. Burial fluxes are denoted ‘B’ and weathering fluxes are denoted ‘W’. A denotes atmosphere and ocean carbon, S denotes oceanic sulphate. G is buried organic carbon, C is buried carbonate, PYR is buried pyrite and GYP is buried gypsum. ΔB and ΔS are the fractionation factors associated with the burial of organic carbon (G) and pyrite (PYR) relative to the ocean/atmosphere fractionation. The assumed isotopic composition of reservoirs for the standard model run are shown underneath the reservoir titles.

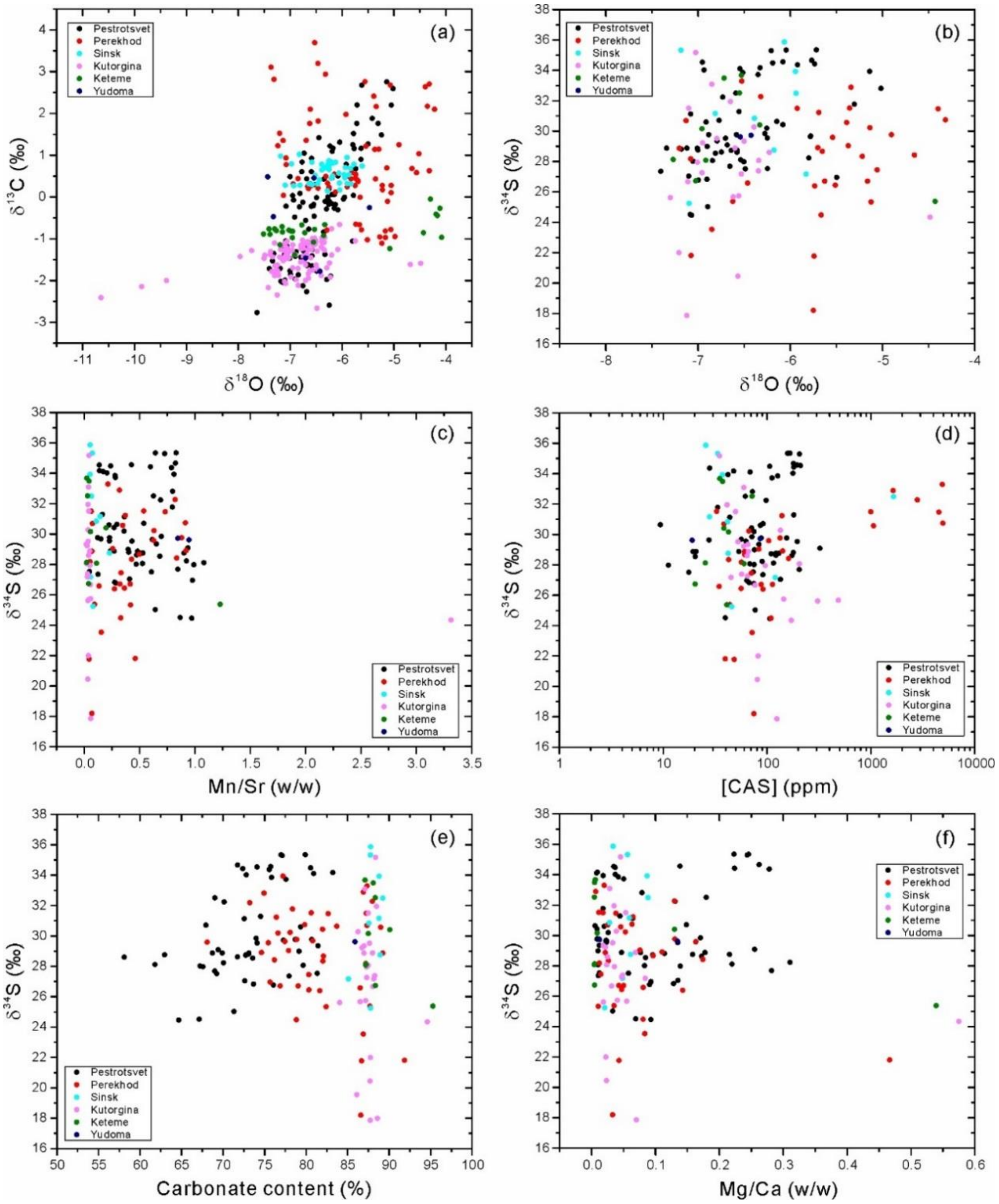

Supplementary Fig. S5. Cross-plots of elemental concentration and isotopic values of carbonates. a. δ^{18}O (‰)–δ^{13}C (‰) ($R^2 = 0.213$). **b.** δ^{34}S (‰)–δ^{18}O (‰) ($R^2 = 0.008$). **c.** δ^{34}S (‰)–Mn/Sr (w/w) ($R^2 < 0.0001$). **d.** δ^{34}S (‰)–[CAS] (ppm) ($R^2 = 0.025$). **e.** δ^{34}S (‰)–carbonate content (%) ($R^2 = 0.002$). **f.** δ^{34}S (‰)–Mg/Ca (w/w) ($R^2 = 0.003$). Different colours represent different stratigraphic formations of the Aldan-Lena rivers sections. Carbonate content (%): weight percentages of HCl-leachable $CaCO_3$ and $CaMg(CO_3)_2$ in carbonate samples. No correlation is observed in any of the cross-plots, indicating minimal digenetic alteration to CAS δ^{34}S.

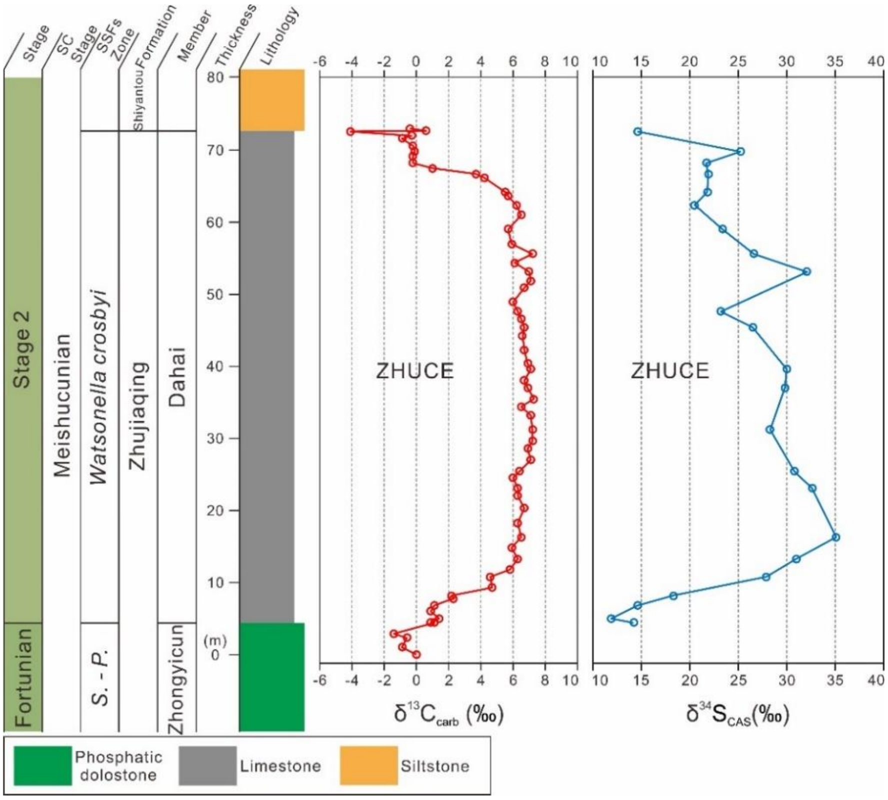

Supplementary Fig. S6. High-resolution carbonate carbon ($\delta^{13}C_{carb}$) and carbonate-associated sulphate sulphur isotope ($\delta^{34}S_{CAS}$) records of early Cambrian Stage 2 to Stage 4 at Xiaotan section, South China. $\delta^{13}C_{carb}$ data are previously published[38]. The regional Stage subdivision is shown next to the global subdivision plan for comparison[38]. SC Stage: South China Stage; Abbreviations: SSFs = small shelly fossils; *S. – P. = Siphogonuchites triangularis – Paragloborilus subglobosus*. ZHUCE = ZHUjiaqing Carbon isotope Excursion. The early Stage 2 ZHUCE event shows positive covariance between $\delta^{13}C_{carb}$ and $\delta^{34}S_{CAS}$ as observed in the Siberian Aldan-Lena rivers sections of Cambrian Stages 2-3, likely representing the first atmospheric oxygenation pulse in the early Cambrian. The ZHUCE event also coincides a rapid diversification event of small shelly fauna[9,39–41].

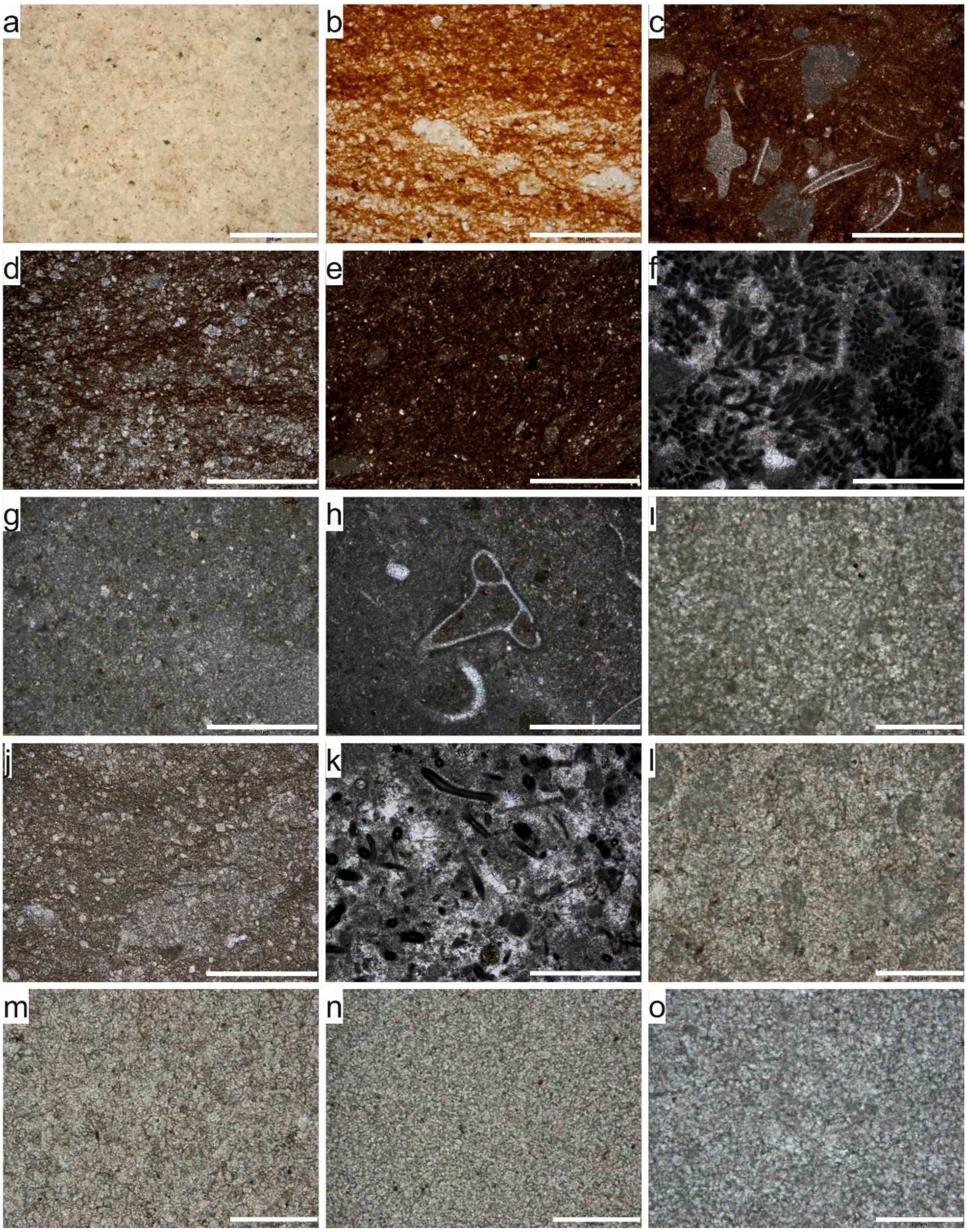

Supplementary Fig. S7. Representative thin-section photomicrograph (plane-polarised light) of carbonate samples used for C-, S-isotope study at Siberian Aldan-Lena rivers sections. (a) micritic sample (IST03, Pestrotsvet Formation, Tommotian Stage) showing fine-grained calcite with minimal siliciclastic content, scale bar = 200 µm. (b) sparitic sample (IST19, Pestrotsvet Formation, Tommotian Stage) with partially recrystallised spars, scale bar = 500 µm. (c) biosparite (IST26, Pestrotsvet Formation, Tommotian Stage) with abundant small shelly fossils (mostly chancelloriids, molluscs and hyoliths) and iron-rich siliciclastic content, scale bar = 1 mm. (d) sparitic sample (IST47, Pestrotsvet Formation, Tommotian Stage) with partially recrystallised spar, scale bar = 500 µm. (e) sparitic sample (ZHU01, Pestrotsvet Formation, Atdabanian Stage) with partially recrystallised spars and iron-rich siliciclastic content, scale bar = 1 mm. (f) micritic carbonate (ZHU09, Pestrotsvet Formation, Atdabanian Stage) with abundant calcimicrobe or microproblematic framework organism, *Gordonophyton*, scale bar = 1 mm. (g-h) microsparite (UKT032, Perekhod Formation, Atdabanian Stage) with the presence of primarily aragonitic chancelloriid *sclerites*, scale bar = 500 µm. (i) coarsely grained dolostone (UKT043, Perekhod Formation, Atdabanian Stage), scale bar = 200 µm. (j) sparitic sample (UKT051, Perekhod Formation, Botoman Stage) with partially recrystallised spars and siliciclastic content, scale bar = 500 µm. (k) biosparitic carbonate (UT03, Perekhod Formation, Botoman Stage) with probable abundant tubular calcimicrobe *Proaulopora*, scale bar = 1 mm. (l) microsparite sample (UKT101, Sinsk Formation, Botoman Stage) contained fine-grained calcite and calcimicrobe fragments, scale bar = 200 µm. (m) microsparite sample (UT27, Sinsk Formation, Botomian) contained fine-grained calcite, scale bar = 200 µm. (n) microsparite sample (LAB56, Kutorgina Formation, Botoman Stage) contained fine-grained calcite, scale bar = 200 µm. (o) microsparite sample (TA28, Keteme Formation, Toyonian Stage) contained fine-grained calcite, scale bar = 200 µm

Isotope excursions/trends	***P***	$\boldsymbol{R^2}$	***RMSE***
III	0.54	0.32	1.64
IV	0.94	0.92	0.96
V	0.60	0.73	1.21
VI	0.64	0.53	1.57
VII	0.74	0.55	2.14
~524–514 Ma	0.50	0.26	2.53
~514–512 Ma	0.076	0.001	4.9

Supplementary Table S1. Statistical correlation parameters for paired short-term δ^{13}C and δ^{34}S excursions and long-term trends. The goodness of fit is indicated by the Pearson index, the coefficient of determination (R^2) and root mean square error (*RMSE*). For Pearson (*P*) and R-square (R^2), closer to one indicate a better correlation between C-S isotopic data; For *RMSE*, smaller number indicate better correlation. ~524–514 Ma: interval when δ^{13}C and δ^{34}S records are positively correlated at Aldan-Lena Rivers sections; ~514–512 Ma: interval when δ^{13}C and δ^{34}S records decoupled.

Flux	Symbol	Rate
Organic C weathering	W(G)	$4 \times 10^{12}\ mol\ yr^{-1}$
Organic C burial	B(G)	Calculated from isotope mass balance
Carbonate weathering	W(C)	$12 \times 10^{12}\ mol\ yr^{-1}$
Carbonate burial	B(C)	$12 \times 10^{12}\ mol\ yr^{-1}$
Pyrite weathering	W(PYR)	$2 \times 10^{12}\ mol\ yr^{-1}$
Pyrite burial	B(PYR)	Calculated from organic C availability
Gypsum weathering	W(GYP)	$1 \times 10^{12}\ mol\ yr^{-1}$
Gypsum burial	B(GYP)	Calculated to maintain a steady state
Parameter	**Symbol**	**Value**
Ocean/atmosphere carbon	A	$3.3 \times 10^{18}\ mol$
Ocean sulphate	S	Varied, present day = $42 \times 10^{18}\ mol$
Isotopic composition of A	δA	Data in this study
Isotopic composition of S	δS	Predicted from model
Isotopic composition of G	δG	Varied, average = -27‰
Isotopic composition of C	δC	Varied, average = 0‰
Isotopic composition of PYR	δPYR	-10
Isotopic composition of GYP	δGYP	30
Fractionation factor: carbon	ΔB	27
Fractionation factor: sulphur	ΔS	40

Supplementary Table S2. List of coupled carbon and sulphur cycle model fluxes and parameters.

Captions for Supplementary Table S3:

Stratigraphic context, age model, litho-, biostratigraphy, sequence stratigraphy and geochemical data for the Aldan-Lena rivers sections. Abbreviations: TA = Tit-Ary; LAB = Labaia; AT = Achchagy-Tuydakh; UT = Ulakhan-Tuoidakh; UKT = Ulakhan-Kyyry-Taas; AKT = Achchagy-Kyyry-Taas; Z Mys and ZHU = Zhurinsky Mys; IST = Isit'; DVO = Dvortsy; SSFs = small shelly fossils; CAS = carbonate-associated sulphate; Carbonate% = total HCl-leachable carbonate content. Siberian Platform sequence stratigraphic data are reconstructed from the Aldan-Lena rivers region[5]. Carbon isotope data numbered as AT, AKT, Z Mys are obtained from the pioneering study[4] to fill the sampling gap in the current study. Sulphur isotope and elemental concentration were obtained from the current study. All elemental analyses represent total 10% HCl-leachable elemental contents of bulk carbonate samples.

Captions for Supplementary Table S4:

Number of total animal species per sampling unit for the Cambrian stages 2-4 at the Siberian Aldan-Lena rivers sections.

Captions for Supplementary Table S5:

Stratigraphic context, litho-, biostratigraphy and C- and S-isotope data for the Xiaotan section, South China. Carbon isotope data are previously published[38]. S-isotope data are from the present study using CAS extraction and isotope analytical protocols described in Methods.

Supplementary References

1. Varlamov, A. I. *et al. The Cambrian System of the Siberian Platform Part 1 : The Aldan-Lena Region*. (PIN RAS, 2008).

2. Astashkin, V. A. *et al*. Cambrian System on the Siberian Platform. Correlation chart and explanatory notes. *Int. Union Geol. Sci. Publ.* 1–133 (1991).

3. Derry, L. A., Brasier, M. D., Corfield, R. M., Rozanov, A. Yu. & Zhuravlev, A. Yu. Sr and C isotopes in Lower Cambrian carbonates from the Siberian craton: A paleoenvironmental record during the 'Cambrian explosion'. *Earth Planet. Sci. Lett.* **128**, 671–681 (1994).

4. Brasier, M. D., Corfield, R. M., Derry, L. A., Rozanov, A. Yu. & Zhuravlev, A. Yu. Multiple δ^{13}C excursions spanning the Cambrian explosion to the Botomian crisis in Siberia. *Geology* **22**, 455 (1994).

5. Zhuravlev, A. Yu. Outlines of the Siberian platform sequence stratigraphy in the Lower and lower Middle Cambrian (Lena-Aldan area). *Rev. Española Paleontol.* 105–114 (1998).

6. Zhuravlev, A. Yu. & Wood, R. A. Anoxia as the cause of the mid-Early Cambrian (Botomian) extinction event. *Geology* **24**, 311 (1996).

7. Brasier, M. D., Rozanov, A. Yu., Zhuravlev, A. Yu., Corfield, R. M. & Derry, L. A. A carbon isotope reference scale for the Lower Cambrian succession in Siberia: report of IGCP Project 303. *Geol. Mag.* **131**, 767 (1994).

8. Dahl, T. W. *et al.* Reorganisation of Earth's biogeochemical cycles briefly oxygenated the oceans 520 Myr ago. *Geochemical Perspect. Lett.* **3**, 210–220 (2017).

9. Peng, S., Babcock, L. E. & Cooper, R. A. The Cambrian Period. in *The Geologic Time Scale 2012* (eds. Gradstein, F. M., Ogg, J. G., Schmitz, M. D. & Ogg, G. M.) 437–488 (Elsevier Science Limited, 2012).

10. Maloof, A. C. *et al.* Constraints on early Cambrian carbon cycling from the duration of the Nemakit-Daldynian–Tommotian boundary δ^{13}C shift, Morocco. *Geology* **38**, 623–626 (2010).

11. Zhang, X. *et al.* Challenges in defining the base of Cambrian Series 2 and Stage 3. *Earth-Science Rev.* **172**, 124–139 (2017).

12. Harvey, T. H. P. *et al.* A refined chronology for the Cambrian succession of southern Britain. *J. Geol. Soc. London.* **168**, 705–716 (2011).

13. Zhuravlev, A. Yu. & Riding, R. (eds.) *The ecology of the Cambrian radiation*. (Columbia University Press, 2001).

14. Yang, C., Li, X., Zhu, M., Condon, D. J. & Chen, J. Geochronological constraint on the

Cambrian Chengjiang biota, South China. *J. Geol. Soc. London.* **175**, 659–666 (2018).

15. Hollingsworth, J. S. Lithostratigraphy and biostratigraphy of Cambrian Stage 3 in Western Nevada and Eastern California. *Museum North. Arizona Bull.* 26–42 (2011).

16. Landing, E. *et al.* Duration of the Early Cambrian: U-Pb ages of volcanic ashes from Avalon and Gondwana. *Can. J. Earth Sci.* **35**, 329–338 (1998).

17. Sundberg, F. A. *et al.* International correlation of the Cambrian Series 2-3, Stages 4-5 boundary interval. *Australas. Paleontol. Mem.* **49**, 83–124 (2016).

18. Butorin, A. *et al. Lena Pillars Nature Park. Potential World Heritage Property*. (Natural Heritage Protection Fund, 2012).

19. Zhuravlev, A. Yu. & Wood, R. A. The two phases of the Cambrian Explosion. *Sci. Rep.* **8**, 1–10 (2018).

20. Zhuravlev, A. Yu. & Naimark, E. B. Alpha, beta, or gamma: Numerical view on the Early Cambrian world. *Palaeogeogr. Palaeoclimatol. Palaeoecol.* **220**, 207–225 (2005).

21. Brand, U. & Veizer, J. Chemical diagenesis of a multicomponent carbonate system -2: stable isotopes. *J. Sediment. Res.* **51**, (1981).

22. Banner, J. L. & Hanson, G. N. Calculation of simultaneous isotopic and trace element variations during water-rock interaction with applications to carbonate diagenesis. *Geochim. Cosmochim. Acta* **54**, 3123–3137 (1990).

23. Allan, J. R. & Matthews, R. K. Isotope signatures associated with early meteoric diagenesis. *Sedimentology* **29**, 797–817 (1982).

24. Lu, M. *et al.* The DOUNCE event at the top of the Ediacaran Doushantuo Formation, South China: Broad stratigraphic occurrence and non-diagenetic origin. *Precambrian Res.* **225**, 86–109 (2013).

25. Shields, G. A. *et al.* Sr, C, and O isotope geochemistry of Ordovician brachiopods: a major isotopic event around the Middle-Late Ordovician transition. *Geochim. Cosmochim. Acta* **67**, 2005–2025 (2003).

26. Maloof, A. C. *et al.* The earliest Cambrian record of animals and ocean geochemical change. *Geol. Soc. Am. Bull.* **122**, 1731–1774 (2010).

27. Fike, D. A., Bradley, A. S. & Rose, C. V. Rethinking the Ancient Sulfur Cycle. *Annu. Rev. Earth Planet. Sci.* **43**, 593–622 (2015).

28. Paytan, A. & Gray, E. T. Sulfur Isotope Stratigraphy. in *The Geologic Time Scale* (eds. Gradstein, F. M., Ogg, J. G., Schmitz, M. D. & Ogg, G. M.) 167–180 (Elsevier, 2012).

29. Gill, B. C., Lyons, T. W. & Frank, T. D. Behavior of carbonate-associated sulfate during meteoric diagenesis and implications for the sulfur isotope paleoproxy. *Geochim. Cosmochim. Acta* **72**, 4699–4711 (2008).

30. Staudt, W. J. & Schoonen, M. A. A. Sulfate Incorporation into Sedimentary Carbonates. *Geochemical Transform. Sediment. Sulfur* **612**, 332–345 (1995).

31. Rennie, V. C. F. & Turchyn, A. V. The preservation of $\delta^{34}S_{SO4}$ and $\delta^{18}O_{SO4}$ in carbonate-associated sulfate during marine diagenesis: A 25 Myr test case using marine sediments. *Earth Planet. Sci. Lett.* **395**, 13–23 (2014).

32. Fichtner, V. *et al.* Diagenesis of carbonate associated sulfate. *Chem. Geol.* **463**, 61–75 (2017).

33. Wotte, T., Shields-Zhou, G. A. & Strauss, H. Carbonate-associated sulfate: Experimental comparisons of common extraction methods and recommendations toward a standard analytical protocol. *Chem. Geol.* **326**–**327**, 132–144 (2012).

34. Vasconcelos, C., McKenzie, J. A., Warthmann, R. & Bernasconi, S. M. Calibration of the $\delta^{18}O$ paleothermometer for dolomite precipitated in microbial cultures and natural environments. *Geology* **33**, 317 (2005).

35. Busenberg, E. & Niel Plummer, L. Kinetic and thermodynamic factors controlling the distribution of SO_3^{2-} and Na^+ in calcites and selected aragonites. *Geochim. Cosmochim. Acta* **49**, 713–725 (1985).

36. Present, T. M., Paris, G., Burke, A., Fischer, W. W. & Adkins, J. F. Large Carbonate associated sulfate isotopic variability between brachiopods, micrite, and other sedimentary components in Late Ordovician strata. *Earth Planet. Sci. Lett.* **432**, 187–198 (2015).

37. Peng, Y. *et al.* Widespread contamination of carbonate-associated sulfate by present-day secondary atmospheric sulfate: Evidence from triple oxygen isotopes. *Geology* **42**, 815–818 (2014).

38. Li, D. *et al.* Carbon and strontium isotope evolution of seawater across the Ediacaran–Cambrian transition: Evidence from the Xiaotan section, NE Yunnan, South China. *Precambrian Res.* **225**, 128–147 (2013).

39. Zhu, M.-Y., Babcock, L. E. & Peng, S.-C. Advances in Cambrian stratigraphy and paleontology: Integrating correlation techniques, paleobiology, taphonomy and paleoenvironmental reconstruction. *Palaeoworld* **15**, 217–222 (2006).

40. Li, G. *et al.* Early Cambrian metazoan fossil record of South China: Generic diversity and radiation patterns. *Palaeogeogr. Palaeoclimatol. Palaeoecol.* **254**, 229–249 (2007).

41. Wang, D. *et al.* Coupling of ocean redox and animal evolution during the Ediacaran-Cambrian transition. *Nat. Commun.* **9**, 2575 (2018).